Geoscience Frontiers 14 (2023) 101542

HOSTED BY

Contents lists available at ScienceDirect

Geoscience Frontiers

journal homepage: www.elsevier.com/locate/gsf

Research Paper

Shallow landslide susceptibility assessment under future climate and land cover changes: A case study from southwest China

Zizheng Guo [a,b,c], Joaquin Vicente Ferrer [b,d,e], Marcel Hürlimann [b], Vicente Medina [b], Carol Puig-Polo [b], Kunlong Yin [c], Da Huang [a,f,*]

[a] School of Civil and Transportation Engineering, Hebei University of Technology, 300401 Tianjin, China
[b] Division of Geotechnical Engineering and Geosciences, Department of Civil and Environmental Engineering, UPC BarcelonaTECH, 08034 Barcelona, Spain
[c] Faculty of Engineering, China University of Geosciences, 430074 Wuhan, China
[d] Institute of Environmental Science and Geography, University of Potsdam, 14476 Potsdam, Germany
[e] Potsdam Institute for Climate Impact Research, 14473 Potsdam, Germany
[f] College of Geological Engineering and Geomatics, Chang'an University, 710064 Xi'an, China

ARTICLE INFO

Article history:
Received 14 March 2022
Revised 10 December 2022
Accepted 17 January 2023
Available online 20 January 2023
Handling Editor: Biswajeet Pradhan

Keywords:
Rainfall-induced landslide
Susceptibility
Climate change
Land cover change
China

ABSTRACT

There is no doubt that land cover and climate changes have consequences on landslide activity, but it is still an open issue to assess and quantify their impacts. Wanzhou County in southwest China was selected as the test area to study rainfall-induced shallow landslide susceptibility under the future changes of land use and land cover (LULC) and climate. We used a high-resolution meteorological precipitation dataset and frequency distribution model to analyse the present extreme and antecedent rainfall conditions related to landslide activity. The future climate change factors were obtained from a 4-member multi-model ensemble that was derived from statistically downscaled regional climate simulations. The future LULC maps were simulated by the land change modeller (LCM) integrated into IDRISI Selva software. A total of six scenarios were defined by considering the rainfall (antecedent conditions and extreme events) and LULC changes towards two time periods (mid and late XXI century). A physically-based model was used to assess landslide susceptibility under these different scenarios. The results showed that the magnitude of both antecedent effective recharge and event rainfall in the region will evidently increase in the future. Under the scenario with a return period of 100 years, the antecedent rainfall in summer will increase by up to 63% whereas the event rainfall will increase by up to 54% for the late 21st century. The most considerable changes of LULC will be the increase of forest cover and the decrease of farming land. The magnitude of this change can reach + 22.1% (forest) and –9.2% (farmland) from 2010 until 2100, respectively. We found that the negative impact of climate change on landslide susceptibility is greater than the stabilizing effect of LULC change, leading to an over decrease in stability over the study area. This is one of the first studies across Asia to assess and quantify changes of regional landslide susceptibility under scenarios driven by LULC and climate change. Our results aim to guide land use planning and climate change mitigation considerations to reduce landslide risk.

1. Introduction

Assessing the impacts of global changes on the environment has been a considerable challenge to the science community (IPCC, 2014; Palmer and Stevens, 2019). Recent studies have shown significant effects of climate and land cover changes on landslide activity in mountainous regions (Ciervo et al., 2017; Gariano et al., 2017; Shu et al., 2019). However, the prediction of these future changes and their potential impacts have remained difficult to quantify on a regional scale.

The effects that climate change (CC) has on the slope stability can be manifold, where the most commonly mentioned pattern is the change of rainfall regime. In the last decades, the increase of the frequency and intensity of extreme rainfall events have been witnessed across the world (Berg et al., 2013; Kharin et al., 2013). These changing conditions consequently affect landslide occurrences in many regions. Some examples are the Mediterranean area (Gariano et al., 2017), East Asia and South Asia (Shou and

* Corresponding author at: School of Civil and Transportation Engineering, Hebei University of Technology, 300401 Tianjin, China.
E-mail address: dahuang@hebut.edu.cn (D. Huang).

https://doi.org/10.1016/j.gsf.2023.101542

Yang, 2015; Kirschbaum et al., 2020), and in New Zealand (Schmidt and Glade, 2003). In addition, changes in cumulative amount and temporal distribution of rainfall can also influence the water balance on hillslopes and increase slope instability (Collison et al., 2000). Additionally, other phenomena that result from climate change can destabilize slopes, including the melting of permafrost and changes in snow-melting regimes due to rising temperatures (Patton et al., 2019), and the upwards shift of treelines in Alpine environments (Bernardie et al., 2021). Thus it can be expected that the climate and its future change can affect the slope stability at different geographical and temporal scales (Gariano and Guzzetti, 2016). This is also recognized by the IPCC special report (Seneviratne et al., 2012), which states that there is high confidence that changes in heavy precipitation will affect landslides across regions. However, due to the lack of data availability and a bias in geographical distribution of current landslide-climate studies (Crozier, 2010; Gariano and Guzzetti, 2016), the specific responses of landslides (e.g. frequency, abundance and spatial location) associated with the projected change in climate remains an open issue (Alvioli et al., 2018). Until the present day, limited efforts have been made to address such issues. An example includes the generative adversarial networks (GAN) to correct limited or imbalanced landslide datasets to improve landslide susceptibility modelling (Al-Najjar et al., 2021; Fang et al., 2021).

The analysis of climate change normally relies on the Global Climate Models (GCMs), which not only can reproduce the characteristics of historical climate, but also predict the future climate scenarios. The assessment of climate change at regional scales requires the downscaling of GCM output to account for local climate dynamics (Hertig and Jacobeit, 2008). Various downscaling techniques have been proposed to obtain regional climate models (RCMs) from global GCMs (Wilby and Wigley, 1997; Kotlarski et al., 2014), such as statistical downscaling and dynamical downscaling methods. The application of methods mentioned above have led to insight on the influence of climate change on regional landslides (Ciervo et al., 2017; Shou and Lin, 2020). However, a constraint that prevents researchers from in-depth analysis of this relationship to landslides is the tempo-spatial variability of climate change.

Another landslide-relevant component of global change is land use and land cover (LULC) change. Not only natural vegetation evolutions but also the change of human land use can drive the land cover changes during a short time (Speich et al., 2020). It is widely known that tree roots have positive effects in consolidating topsoil and stabilizing slopes, therefore afforestation can improve the stability conditions of bare areas (Schmaltz and Mergili, 2018; Lan et al., 2020). In contrast, deforestation reduces the slope stability mainly from two aspects. On one side, the loss of canopy coverage allows rainfall to directly infiltrate into the slope and soil layers can be saturated more quickly (Schmaltz et al., 2017). While, the root cohesion and shear strength of the soil profiles decreases constantly after the forest cutting (Runyan and D'Odorico, 2014). Evident changes of LULC have been observed in many regions since the last century, such as the rapid expansion of urban areas in Asia (Xiao et al., 2006; Chen et al., 2019), the abandonment of agricultural land in mountainous areas of Europe (MacDonald et al., 2000), and a large amount of forest loss in South America (Salazar et al., 2015). Given that the driver forces of LULC, especially the socioeconomic factors, exhibit rapid change (Roura-Pascual et al., 2005), and the rate of conversion of natural vegetation can be high (Wang et al., 2006), it is of upmost importance to consider the future LULC dynamics for the risk mitigation of slope mass movements.

At a regional scale various techniques have been applied to assess the influence of the distribution of different LULC types on slope stability. This is mainly conducted through statistical methods, physically-based models, and heuristic methods (Reichenbach et al., 2014; Shu et al., 2019; Bernardie et al., 2021). Among them, physically-based models are considered to have an advantage compared with statistical models, because they allow the integration of hydraulic-mechanical parameters into the model, which are necessary to evaluate the effects of LULC types (Van Beek and Van Asch, 2004). Certainly, this type of model has also drawbacks; critically, data collection is often an operational challenge over large areas. Therefore, the widely adopted assumption regarding the homogeneity of soil properties is closely related to modelling uncertainty (Tofani et al., 2017).

Although it is well known that changes in precipitation and LULC have a range of effects on landslides, both factors are generally studied separately. Available studies on the combined impacts of these two changes are very limited (e.g., Grandjean et al., 2018; Bernardie et al., 2021; Hürlimann et al., 2022), and uncertainties related to future predictions are significant. In particular, new studies in Asia, South America, and Africa are highly recommended to fill the gap (Gariano and Guzzetti, 2016). Additionally, many studies have used changes in landslide susceptibility (LA) to reflect the impacts of environmental changes on landslide activity. The concept of LA can represent the spatial probability of landslide occurrence in a region, and it normally involves the analysis of the correlation between historical landslides and environment factors (Fell et al., 2008). During the past decade, many GIS-based methods/techniques have been proposed and applied for regional landslide susceptibility modelling (Althuwaynee and Pradhan, 2017; Dikshit et al., 2020; Rafiei Sardooi et al., 2021), which become useful tools on this topic.

The main goal of this study is to improve our understanding of the relationship between the environmental changes and landslide activity at a regional scale. The specific objectives include: (i) a detailed analysis of the historical rainfall regime and future prediction, (ii) determination of future LULC scenarios, and (iii) a regional landslide susceptibility quantification under different future scenarios. The Wanzhou region in China was taken as the study area, which seems to be the first time that such an assessment and comparison of the impact of LULC and climate changes on landslide susceptibility in Asia. In details, LULC prediction and two rainfall conditions (antecedent rainfall and extreme daily rainfall) were both considered in assessing the combined slope stability in the study region until the late 21st century, in contrast to the assessment of separate conditions used in previous studies. A multi-model ensemble was developed to predict future changes in extreme and seasonal rainfall magnitudes with regional climate model simulations. The increase of temperature associated with global warming was also included to estimate the antecedent water recharge in the future.

The structure of the paper is organized as follows: in Section 2 and 3, we introduce the study site, methodologies and datasets. Section 4 presents and analyses the test results, followed by Section 5 where the results are discussed and compared with similar studies. In Section 6, we present our conclusions.

2. Study area

2.1. General settings

The study zone encompasses the Wanzhou County (30°24′25″N, 107°52′22″E to 31°14′58″N, 108°53′25″E) from nearby the Three-Gorges Reservoir area (China) covering an area of 3457 km^2 (Fig. 1a). The area is part of the north-eastern Sichuan Basin which is highly dissected, and is formed in the Yangtze River valley belt. It is characterized by a parallel ridge-and-valley area and surrounded by a typical hilly and mountainous landscape (Xiao et al., 2019). The elevation in the region

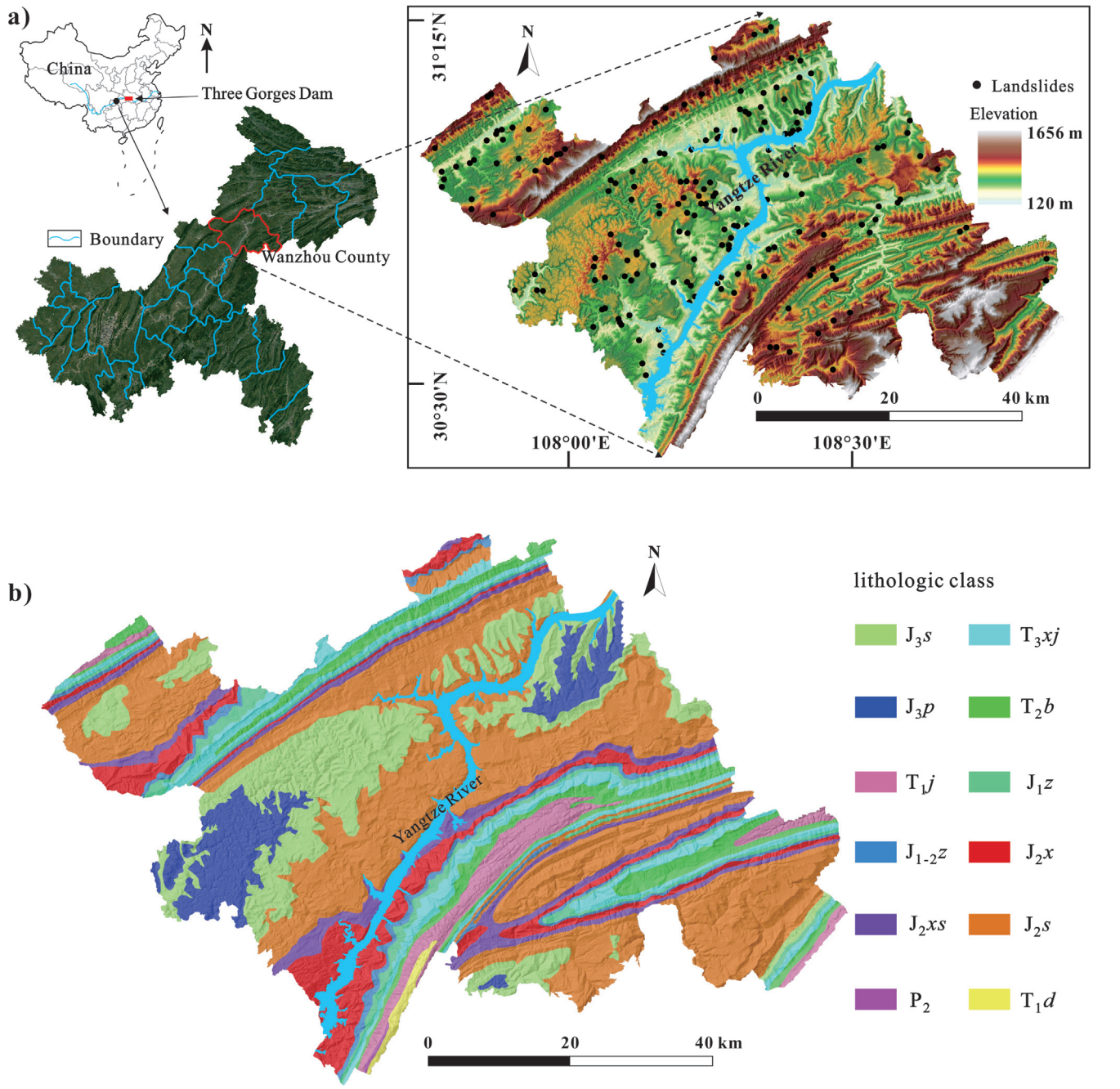

Fig. 1. (a) Location of Wanzhou County in China. The base map is 30 m digital elevation model (DEM) where the black dots show the spatial distribution of the shallow landslides used in this study. (b) The lithologic map of the study area (see text for explanation of the legend).

ranges from 120 m a.s.l. to 1656 m a.s.l., and overall the southeast is higher than the northwest.

The geological settings of the region consists of 7 sedimentary strata with ages between 300 Ma and 3 Ma, including middle Permian (P_2), Triassic (T_1, T_2, and T_3) and Jurassic (J_1, J_2 and J_3) stratum (Fig. 1b). Most of these geologic units have sub-horizontal layering and several vertical sets of subunits. For instance, the middle Jurassic (J_2) is the most widely distributed strata in the area, which can be divided into three subunits: the Xintiangou Formation (J_2x), the lower Shaximiao Formation (J_2xs) and upper Shaximiao Formation (J_2s) (Huang et al., 2017; Wang et al., 2017). The most important difference among these strata is the lithology, of which the sandstone and mudstone are the most common, followed by Triassic limestone. The Quaternary can be represented by colluvial deposits in the southern part of the area, and by the silty clay with gravels which covers the bedrock.

The area is found in a subtropical monsoon climate with a mean temperature of 18 °C and with average annual rainfall greater than 1200 mm. Meanwhile, a clear temporal difference in rainfall pattern can be seen: the dry season is between November and March. The rainy season extends from May to September, and normally yields a maximum total precipitation in July and August (Guo et al., 2020; Li et al., 2021).

The resident population in the area is approximately 1.6 million and the settlements mainly distribute on the banks of the Yangtze River, which is the biggest and longest river in China (Fig. 1). Critically, the northeast is highly populated and urbanized.

2.2. Description and reanalysis of landslide inventory

Wanzhou County spreads over a mixture of river and hilly landscape. The combination of such susceptible geomorphology and seasonal rainfall may be the reason why plenty of landslides have been recorded in this region.

Landslide inventory mapping is a basic step for regional landslide susceptibility assessment (Guo et al., 2021). In this study, the landslide inventory was provided by Wanzhou Institute of Geological Environment Monitoring. A total of 665 landslides were recorded (Xiao et al., 2019), and their detailed information were collected through field work and archived into landslide reports. The depths of these landslides range from approximately 1 m to greater than 30 m, and most of them occurred in the colluvial deposits (Liu et al., 2016). The volume of landslides varies significantly, with volumes ranging from 200 m^3 to approximately 10^7 m^3 (Guo et al., 2019; Xiao et al., 2019).

These landslides can be roughly divided into three categories (Cruden and Varnes, 1996; Hungr et al., 2014): (i) shallow landslides in a rotational or translational form, most of which are associated with the upper soil layer; (ii) large deep-seated landslides with thickness of more than 10 m; (iii) a small amount of rockfalls, accounting for approximately 3.9% of the total landslides in the region. The model we used to calibrate parameters in this study (see section 3.3 for details) mainly considers the rainfall as the landslide triggering mechanism (Medina et al., 2020). Hence, only type (i) of landslides were taken into account for further susceptibility simulations, whereas deep-seated failures and rockfalls were not considered. Next, considering the landslide inventory temporally spans over decades and data availability, we filtered rainfall-induced shallow landslides during 1995 and 2005 (Fig. 1a) for parameter calibration. There were 186 shallow landslides in the final inventory in this study.

3. Methodologies and data

3.1. Overall workflow

There are four main parts included in the workflow of this study (Fig. 2): (i) the rainfall analysis of the study area, (ii) the calibration of parameters for landslide susceptibility modelling, (iii) the prediction of future changes in climate and LULC, and (iv) the assessment and comparison of regional landslide susceptibility under the two changing conditions.

The first part focuses on the present rainfall condition of the study area. We analyzed the spatial variability of the summer seasonal rainfall and extreme daily rainfall by using high-resolution gridded precipitation data. The preliminary result of this step is to create two types of present rainfall distributions, namely antecedent rainfall (P_a) and event rainfall (P_e). The law of water balance states that only part of rainfall can infiltrate into the soil layer and result in recharge. Hence, in order to obtain the effective antecedent recharge (P_a), the effective recharge ratio (*ERR*) was calculated, which was defined as the percentage of q_a out of the *Pa*. The q_a is defined as a reduced percentage of the precipitation due to the runoff and evapotranspiration, and can also be considered as the effective antecedent water infiltration into the soil layer during a mid to long-term period previous to the event rainfall. It provides the initial condition for landsliding. The P_e considers the effect of the short-term rainfall event and represents the boundary condition for landsliding. It is related to the vertical flow method which can be used to calculate the increase of water table triggered by a storm event (Medina et al., 2020).

In the second step, the rainfall-induced shallow landslides between 1995 and 2005 in Wanzhou County were used to calibrate the parameters involved in the stability model. The reason why we didn't apply the entire landslide inventory is that the parameters used in stability modelling are both variable and static (see section 3.3 for details). Hence, it is necessary to use the landslides occurring during a shorter time period instead of a long one. Specifically, a total of seven parameters (six soil properties and root cohesion) were fixed in the phase of the study (see section 3.3 for more details). Selecting the rainfall return period to model an inventory is challenging. In case that the inventory includes historical events, the return period could be linked to the oldest event identified. An inventory created with the ongoing events is different. If the return period of the triggering precipitation is precisely measured, the maximum of those values could be used in the model. In cases where data is not available, a more heuristic approach is required. In our case the inventory includes 11 years. The return period that has the probability 0.5 of being exceeded in 11 years is 16.5 years. Hence, the event rainfall map corresponding to 20 years was selected for the calibration simulations, whereas 10 years was discarded as being too low.

During the next phase of the study, the future scenarios of climate and LULC were determined. For comparison, the present conditions of LULC, q_a (herein called $q_{a\text{-}pres}$) and P_e (herein called $P_{e\text{-}pres}$) were defined as the reference scenario. Two future periods (herein called mid, and late XXI century) were selected, and the climate and LULC changes for these two periods were predicted individually without considering their interaction. It should be noted that the prediction regarding the climate change is simplified to changes in rainfall for this study. Different from previous studies (e.g., Hürlimann et al., 2022), both antecedent conditions and event rainfall are considered variable over time, thus not only event rainfall but also the changes in effective antecedent recharge are predicted. Furthermore, the method for future rainfall prediction is another important improvement in this study. We used a high-resolution gridded precipitation dataset and an ensemble derived from statistical downscaling using extreme value statistics to improve the prediction of regional climate model outputs rather than a pixel-based daily rainfall series and trend analysis for the future frequency (Hürlimann et al., 2022). The methodology and procedure applied in this step will be comprehensively described in this section. In general, we calculated the climate change factor (*CCF*), which is defined as the ratio of magnitude in future rainfall to present rainfall in this study. Future event rainfall can be obtained by using the present map ($P_{e\text{-}pres}$) and *CCF*, whereas the prediction of effective antecedent recharge needs the *ERR* for the future scenario in addition to the present map ($P_{a\text{-}pres}$) and *CCF*. The output of the LULC prediction is directly a LULC map.

Finally, the landslide susceptibility was calculated for each scenario by using the outputs from previous steps. A Total of 7 scenarios (Table 1) were determined, including a reference scenario which used the present LULC and rainfall conditions and 6 future scenarios. All the scenarios were calculated for the return period of 100 years (T_{100}). By comparing with the reference scenario, not only the individual impacts of climate and LULC changes, but also their combined impacts were assessed and quantified.

3.2. Analysis of present rainfall conditions

The analysis of rainfall within the study area utilized gridded precipitation data to analyse the spatial variability and the distribution characteristics of antecedent rainfall conditions and extreme daily rainfall events. This section will introduce the spatial data products and approaches used to obtain effective antecedent recharge (q_a) and event rainfall (P_e) maps for the present period.

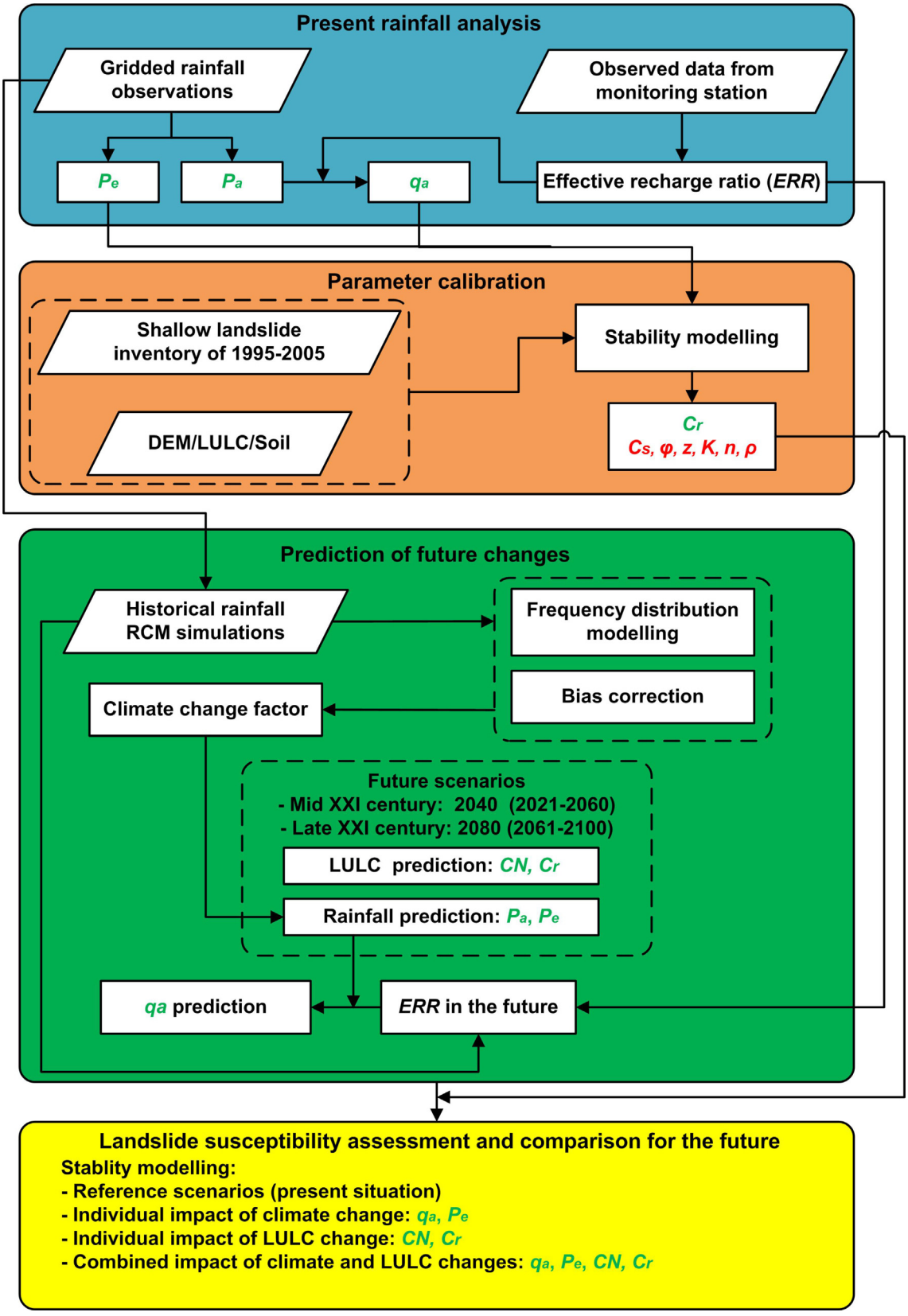

Fig. 2. The overall workflow of this study. Parameters marked in green are variable over time related to climate and vegetation change. Parameters marked in red are static parameters related to soil properties. Detailed parameter abbreviations are explained in the section 3.3.

Table 1
Definition for different scenarios considering LULC and climate changes. $P_{a\text{-}pres}$ represents the present antecedent rainfall condition whereas $P_{e\text{-}pres}$ represents the present event rainfall of Wanzhou County. CCF_i is the climate change factor for the two types of rainfalls in different time periods i (mid and late XXI century). ERR_i is the effective recharge ratio for the two time periods i.

No.	Scenario	LULC (year)	Effective antecedent recharge, q_a	Event rainfall, P_e
1	Reference scenario (present)	2000	$P_{a\text{-}pres}{}^{*}\ ERR_{pres}$	$P_{e\text{-}pres}$
2	Mid XXI century LULC	2040	$P_{a\text{-}pres}{}^{*}\ ERR_{pres}$	$P_{e\text{-}pres}$
3	Late XXI century LULC	2080	$P_{a\text{-}pres}{}^{*}\ ERR_{pres}$	$P_{e\text{-}pres}$
4	Mid XXI century CC	2000	$P_{a\text{-}pres}{}^{*}\ CCF_{mid\text{-}Pa}{}^{*}\ ERR_{mid}$	$P_{e\text{-}pres}{}^{*}\ CCF_{mid\text{-}Pe}$
5	Late XXI century CC	2000	$P_{a\text{-}pres}{}^{*}\ CCF_{late\text{-}Pa}{}^{*}\ ERR_{late}$	$P_{e\text{-}pres}{}^{*}\ CCF_{late\text{-}Pe}$
6	Mid XXI century LULC + CC	2040	$P_{a\text{-}pres}{}^{*}\ CCF_{mid\text{-}Pa}{}^{*}\ ERR_{mid}$	$P_{e\text{-}pres}{}^{*}\ CCF_{mid\text{-}Pe}$
7	Late XXI century LULC + CC	2080	$P_{a\text{-}pres}{}^{*}\ CCF_{late\text{-}Pa}{}^{*}\ ERR_{late}$	$P_{e\text{-}pres}{}^{*}\ CCF_{late\text{-}Pe}$

3.2.1. Description of precipitation dataset

Precipitation data representing the spatial variability of the study area was determined to be essential, given the regional scale of the test area, and dispersed locations of the events in the landslide inventory. Thus, a high-resolution gridded precipitation product derived from satellite observations and interpolated rain gauge data was consideration to analyse the rainfall-triggering characteristics within the study area.

This study utilized the spatially distributed China Meteorological Forcing Dataset (CMFD) gridded precipitation dataset with a temporal resolution of 3 h and a spatial resolution of 0.1° (Yang and He, 2019). The CMFD precipitation dataset was derived from the integration of multi-satellite remote sensing products, reanalysis datasets and rain gauge observations from 1979 to 2018. The algorithm for the creation of the precipitation dataset utilized a monthly scale for interpolation, due to a smoother spatial distribution compared to results from sub-daily interpolation. The sub-daily values were obtained through the integration of Chinese Meteorological Agency (CMA) station observations to gridded data from the Global Land Data Assimilation System (GLDAS) and Tropical Rainfall Measuring Mission (TRMM) at 0.1°. The interpolated sub-daily precipitation rate was then proportionally adjusted to the interpolated precipitation estimates at a monthly scale to obtain the spatial and temporal characteristics described above (He et al., 2020). Daily precipitation at a spatial resolution of 0.1° was selected from the CMFD dataset for the rainfall analysis and reconstruction of inventory precipitation characteristics for this study.

3.2.2. Analysis of the antecedent condition

The determination of the landslide-triggering antecedent rainfall period is highly dependent on the groundwater conditions. Therefore, there is a prevalence in variety of methodologies for incorporating antecedent rainfall conditions in shallow landslide susceptibility thresholds (Segoni et al., 2018). The causal relationship between the summer season for a majority of landslides occurrences in Wanzhou with the significant accumulated monthly rainfall beginning from May suggests significant influence of antecedent rainfall at monthly scale on shallow landslide triggering (Guo et al., 2019). Hence, the 30-day antecedent rainfall between May to August was selected to represent a significant period by which the recharge prior to landslide would be estimated.

The mean seasonal rainfall (MSR) in the summer was computed for the months of May to August for the years of 1979 to 2018. As seen in Fig. 3, the resulting MSR represents the present antecedent rainfall (P_a) condition in Wanzhou County, with the study area having a MSR range of 5.95 mm/d to 6.22 mm/d.

Next, the EasyBal software (UPC, 2021) designed by the Division of Geotechnical Engineering of the UPC was utilized to calculate the effective recharge ratio (*ERR*), which was defined as the ratio of effective antecedent recharge (q_a) to antecedent rainfall (P_e). The software can evaluate water balance per unit of soil area, and its input data includes precipitation, potential evapotranspiration (or ETP), temperature (minimum, maximum and mean values) and irrigation. In this study, daily data was obtained from a monitoring station within the Wanzhou region with the coordinates 30.77°N, 108.40°E, and located at 187 m asl (CAS, 2021). The irrigation data was lacking, so we set it as 0. The monthly effective antecedent rainfall and *ERR* values from 1995 to 2005 is shown in Fig. 4. The mean ERR values in summer was 11.7%, which means that 11.7% of antecedent rainfall was estimated to be effective recharge into the soil layer in the region. This ratio was considered as a constant value for the entire area, so the effective antecedent recharge (q_a) map can be obtained by multiplying the antecedent rainfall map by 0.117.

3.2.3. Frequency distribution modelling for event rainfall

The application of extreme value statistics (EVS) was implemented to determine the frequency distribution of extreme daily rainfall events with the potential to trigger landslides within the study area. A Block Maxima approach was utilized to derive the probability distribution functions of extreme rainfall events from the daily precipitation measurements in CMFD dataset. This approach equally divides the daily precipitation series into prescribed time periods, and from these blocks extracts the maximum values:

$$Mn = max\{P_1, ..., P_n\} \tag{1}$$

where a sequence of n daily precipitation P variables were taken into consideration. The maximum values Mn obtained from the blocks of the equation above are then utilized to obtain a probability distribution function. Although annual maxima is typically considered for hydrological applications, studies demonstrate that the monthly maxima can more precisely derive annual return levels when taking seasonality into consideration (Rust et al., 2009; Fischer et al., 2018). The probability distribution function selected to obtain the annual return levels from the monthly maxima was the Gumbel distribution. The Gumbel distribution probability density function (*PDF*) $f(x)$, and cumulative density function (*CDF*) $F(x)$ are as Eqs. (2) and (3):

$$f(x) = (\frac{1}{\alpha})exp[-(\frac{x-\beta}{\alpha}) - exp(-(\frac{x-\beta}{\alpha}))] \tag{2}$$

$$F(x) = exp[-exp(-\frac{x-\beta}{\alpha})] \tag{3}$$

where β is the location parameter and α is the scale parameter. The relationship between the mean, location and scale parameter is given by Eq. (4):

$$\mu = \beta + 0.5772\alpha \tag{4}$$

The parameters α and β were calculated through maximum likelihood estimation (MLE). The distribution parameters θ estimated by maximizing the likelihood function Eq. (5):

$$L(\theta) = \prod_{i=1}^{n} f(x_i|\theta) \tag{5}$$

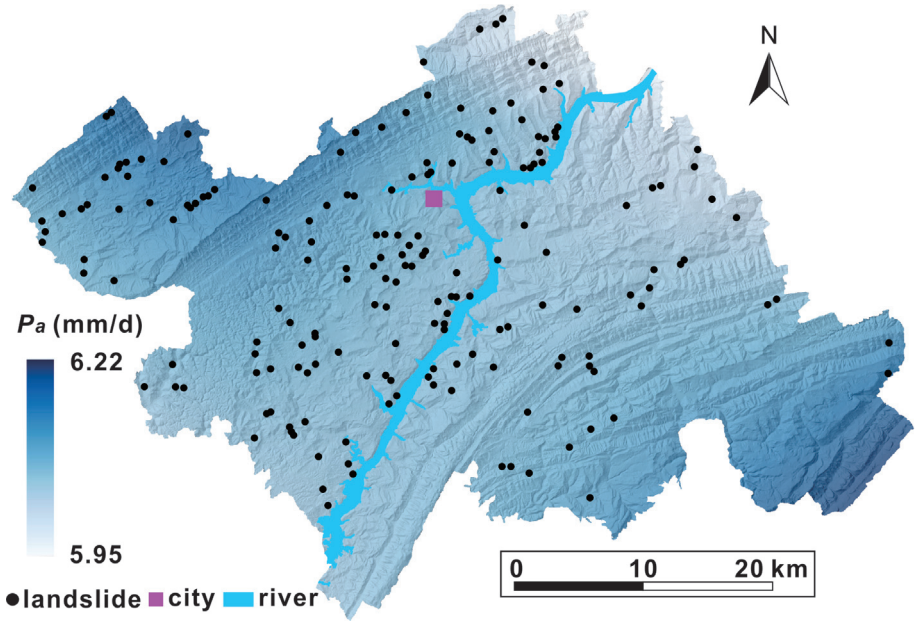

Fig. 3. The mean seasonal rainfall distribution of the study area from May to August during the period from 1979 to 2018.

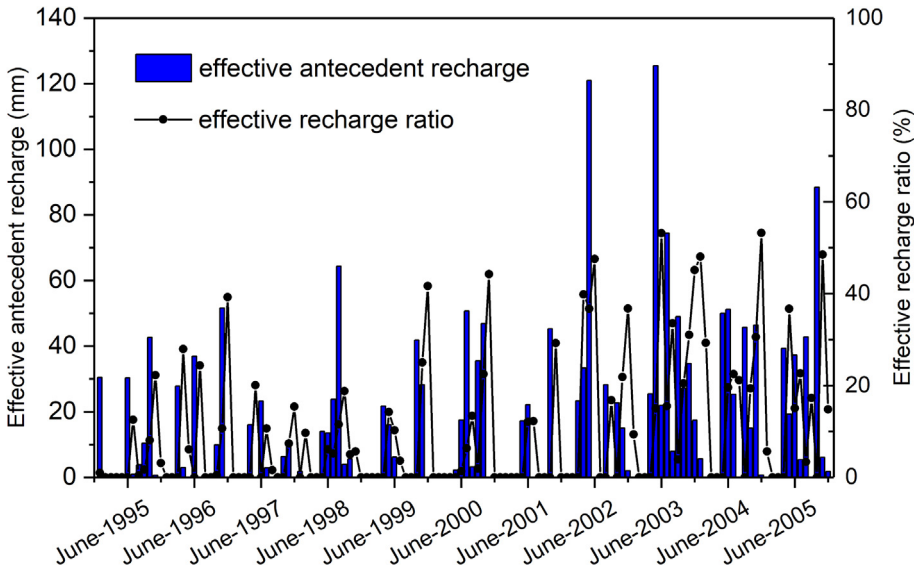

Fig. 4. Monthly effective antecedent recharge and *ERR* obtained from EasyBal software during 1995 and 2005.

where x_i is the n observations of variable X and $f(x_i|\theta)$ is the density function of the distribution. The algorithm implementing the estimation methods utilized the fitdistrplus R package (Delignette-Muller and Dutang, 2015).

The extreme rainfall rates R_T in mm/d given the recurrence period of T years were determined by Eq. (6):

$$R_T = \mu - \alpha[lnln(\frac{T}{T-1})] \quad (6)$$

The procedure for estimating the parameters of the Gumbel distributions based on the CMFD dataset with the MLE was conducted across the study area. A distribution for each pixel derived from the CMFD within the study area was derived using the procedure described above to attain the spatial distribution of extreme rainfall for different return periods with Eq. (6). The validation of the estimated Gumbel distributions was performed with the goodness-of-fit tests: Kolmogorov-Smirnov (KS), Anderson-Darling (AD) and the Cramer-von-Mises (CVM) criterion, evaluated at a confidence level of 95% (Ferrer et al., 2022).

3.3. Parameter calibration

3.3.1. General aspect

In this study, the Fast Shallow Landslide Assessment Model (FSLAM), which is a physically-based model proposed by Medina et al. (2020) was applied. It can calculate the water table in the soil layer by considering both the effective antecedent recharge (q_a) and the event rainfall (P_e). Moreover, to overcome the uncertainty of soil properties over a large area, a stochastic approach of input parameters is used in the FSLAM model, which allows output of probability of failure (*PoF*) at each cell.

There are total ten parameters included in the FSLAM model, namely the effective cohesion of soil (C_s), root cohesion (C_r), friction angle of soil (φ), density of the saturated soil (ρ_s), soil depth (z), horizontal hydraulic conductivity (K), soil porosity (n), curve number (CN) of land cover, effective antecedent recharge (q_a), and the event rainfall (P_e). Among them, six parameters are related to the soil type (C_s, φ, ρ_s, K, n, and z), two are associated with the vegetation (C_r and CN), and two are rainfall-related (q_a and P_e). The parameters related to soil type are static, whereas the parameters affected by vegetation are dynamic over time.

The rainfall-induced shallow landslides in Wanzhou between 1995 and 2005 were used for the parameter calibration. The stability modelling was performed by using the FSLAM model to fit the 186 landslide inventory points in this period. During this calibration phase, all the soil properties (C_s, φ, ρ_s, K, n, and z) and root cohesion (C_r) were adjusted.

3.3.2. Input data and stability modelling

The objective of the parameter calibration phase is to fix all the stability parameters (soil properties and root cohesion) and the curve number (CN). We determined the initial input values of these parameters according to existing literature and expert criteria (USDA, 1986; Fanelli et al., 2016; Bicocchi et al., 2019; Medina et al., 2020; Geotechdata, 2021). Given the number of landslides and availability of input data, the time period from 1995 to 2005 was selected, and a total of 186 rainfall-induced shallow landslides were identified in the inventory. Next, the FSLAM modelling was iteratively carried out to fit the 186 landslides in this period. During this stage, we focused on the accuracy of the stability modelling by applying receiver operating characteristic (ROC) techniques.

There are five necessary input rasters for the FSLAM model, namely DEM, soil properties, LULC, q_a and P_e. The DEM (Fig. 1a) was downloaded from the website of Geospatial Data Cloud (2021) with a resolution of 30 m. The LULC map of 2000 (Fig. 5a) was downloaded from the Resource and Environment Science and Data Center of Chinese Academy of Sciences (CAS, 2021) and then reclassified into 10 categories. The soil map (Fig. 5b) was from the same source (CAS, 2021) and reclassified into 9 categories according to the World Reference Base (IUSS Working Group WRB, 2014). The present distribution of effective antecedent recharge (q_a) (Fig. 5c) and event rainfall (P_e) (Fig. 5d) were determined as described in section 3.2.2 and 3.2.3, respectively.

All the rasters above were prepared with a cell size of 30 m, and there was a total of approximately 8 million cells in the entire region. Since FSLAM applies a simplified method to calculate stability, only 2 min was necessary to run the model by using an ordinary personal laptop. This was important for improving the efficiency of the study, especially when an iterative method was used to perform calibration procedure.

Finally, the best-fit parameters are shown in Tables 2 and 3, and the obtained landslide susceptibility map using these values is presented in Fig. 6a. To evaluate the accuracy of the simulation, 5000 random points were selected within the area and the ROC curve was obtained by computing true positive (TP) rate versus false positive (FP) rate at different PoF thresholds. Seen in Fig. 6b, the accuracy represented by the area under the curve of 0.79 indicated that the model's performance was satisfactory.

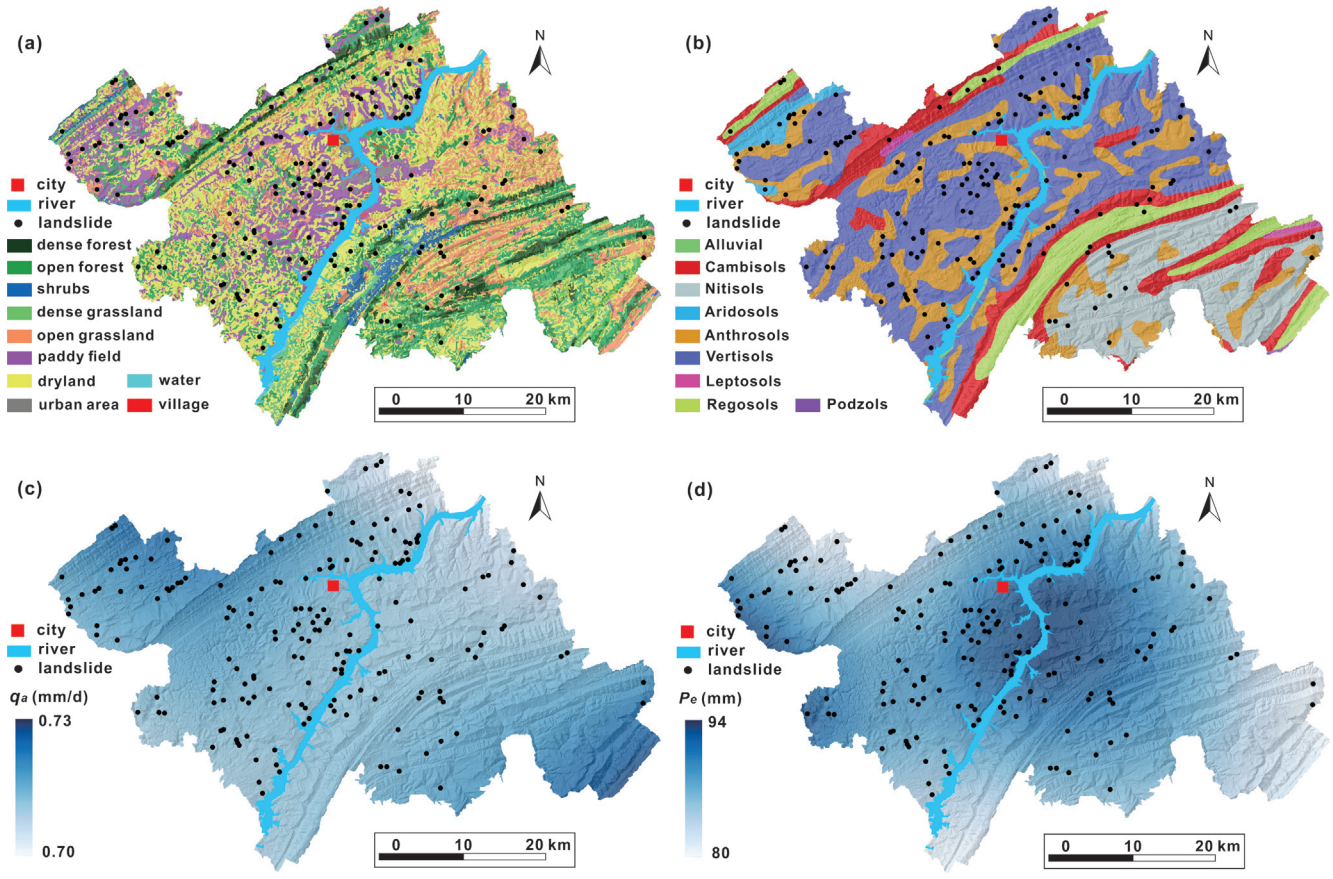

Fig. 5. Input rasters of the stability modelling for the parameter calibration: (a) LULC map in 2000, (b) soil map of the study area, (c) present effective antecedent recharge, (d) present event rainfall with the return period of 20 years.

Table 2
The soil properties obtained from the calibration phase. HSG represents hydrologic soil group (USDA, 2007).

Lithological class	C_s -min/max (kPa)	φ-min/max (°)	h (m)	K (m/s)	n (-)	ρ (kg/m^3)	*HSG* (-)
Alluvial	0/3	35/45	1	1×10^{-3}	0.3	2000	A
Cambisols	0/3	30/40	0.9	1×10^{-5}	0.3	2000	C
Nitisols	0/5	25/35	0.8	1×10^{-6}	0.3	2000	D
Aridosols	0/3	30/40	0.7	1×10^{-4}	0.3	2000	C
Anthrosols	0/1	25/35	0.5	1×10^{-5}	0.3	2000	D
Vertisols	0/1	25/35	0.7	1×10^{-4}	0.3	2000	A
Leptosols	0/5	30/40	0.75	1×10^{-5}	0.3	2000	D
Regosols	0/3	25/35	0.7	1×10^{-5}	0.3	2000	B
Podzols	0/5	25/35	0.6	1×10^{-6}	0.3	2000	D

Table 3
Best-fit values of curve number and root cohesion resulted from the calibration phase.

LULC	C_r -min/max (kPa)	*CN-A* (-)	*CN-B* (-)	*CN-C* (-)	*CN-D* (-)
dense forest	0/8	36	60	73	79
open forest	0/5	45	66	77	83
shrubs	0/5	43	65	76	82
dense grassland	0/3	49	69	79	84
open grassland	0/3	68	79	86	89
paddy field	0/1	63	74	82	85
dryland	0/1	62	71	78	81
water	999/999	100	100	100	100
urban area	0/1	54	70	80	85
village	0/1	77	86	91	94

Then, the *PoF* = 0.5 was selected as the threshold to distinguish the cells as stable or unstable (Camilo et al., 2017), and the confusion matrix was analysed (Table 4). The accuracy (*ACC*) value calculated at this threshold was 0.664. It is slightly lower than some previous studies (Maximum accuracy is 0.71 in Camilo et al. (2017); and accuracy is 0.705 in (Medina et al., 2020)). However, considering the simplified method used by the FSLAM model and uncertainty level of the parameters in such a large study area the obtained accuracy was acceptable.

3.4. Analysis of climate and LULC changes

3.4.1. Prediction of climate change

In the present study, the climate change prediction is principally focused on the change in rainfall, and its main objective is to provide two input parameters for the landslide susceptibility modelling in future scenarios, namely effective antecedent recharge (q_a) and event rainfall (P_e).

The Phase 5 Coupled Intercomparison Modelling Project (CMIP5) outputs (Taylor et al., 2012), performed under the Coordinated Downscaling Experiment (CORDEX) project's East Asian domain, was applied to obtain the rainfall projections for the future. It should be stated that the rainfall obtained here is the antecedent rainfall (P_a) and event rainfall (P_e). Given the inherent uncertainties of the climate change models, a multi-model ensemble was developed to obtain robust predictions. The 4 Regional Climate Model outputs used 3 Global Climate Models as boundary conditions were utilized to construct the ensemble (Table 5).

The selection of the RCM outputs included in the ensemble was based on a review of studies indicating reasonable representation of climate over China and the Yangtze River Basin by the REMO2015 and RegCM4 (Xu et al., 2016; Gao et al., 2017; Huang et al., 2021). The boundary conditions of these RCMs were driven by the United Kingdom's Met Office Hadley Centre HadGEM2-ES (Jones et al., 2011) and the Max Planck Institute for Meteorology Earth system model (MPI-ESM) (Ilyina et al., 2013). Each RCM member was assigned equal weight to avoid uncertainty derived from the process of weighing assessing climate model performance (Christensen et al., 2010). Two different time periods were determined as the future scenarios, as mentioned in section 3.1: the middle 21st Century from 2021 to 2060, and the late 21st Century from 2061 to 2100. The P_a and P_e in these scenarios were predicted under the future Representative Concentration Pathways (RCP) 8.5 (Moss et al., 2008).

Under the RCP 8.5 scenario, a projected increase in seasonal precipitation and extreme rainfall during the summer season has been observed in the analysis climate change model simulations by the middle 21st Century (Gu et al., 2018; Qin et al., 2021; Tong et al., 2021; Ferrer et al., 2022). An increase in extreme rainfall is anticipated in the late 21st century, the reliability of these extreme rainfall projections is reflected in significant variation (Ferrer et al., 2022) that reflects the limited ability of the GCMs to reproduce the Asian monsoon (Freychet et al., 2015; Xu et al., 2018).

The bias correction was performed on RCM outputs to extract the climate signals for two types of rainfall (P_a and P_e). The main objective of this step is to remove systematic errors resulting from the differing climate model configurations. We used a quantile delta mapping (QDM) bias correction method to obtain the bias-corrected rainfall for the two future scenarios.

The magnitude of climate change was determined by the ratio between corrected future rainfall and historical rainfall. As previously mentioned, a climate change factor (CCF) was defined as following Eq. (9):

$$CCF_{i,\,T} = \frac{P_{F,\,T}}{P_{H,\,T}} \tag{7}$$

where $CCF_{i,T}$ represents the climate change factor of P_a or P_e with a return period of T, i is the time period (middle or late 21st century), $P_{F,T}$ is the bias-corrected future rainfall with a return period of T, and $P_{H,T}$ is the bias-corrected historical rainfall with the return period of T. Hence, the P_a and P_e for the future scenarios can be obtained by multiplying corresponding CCF value to the reference scenario.

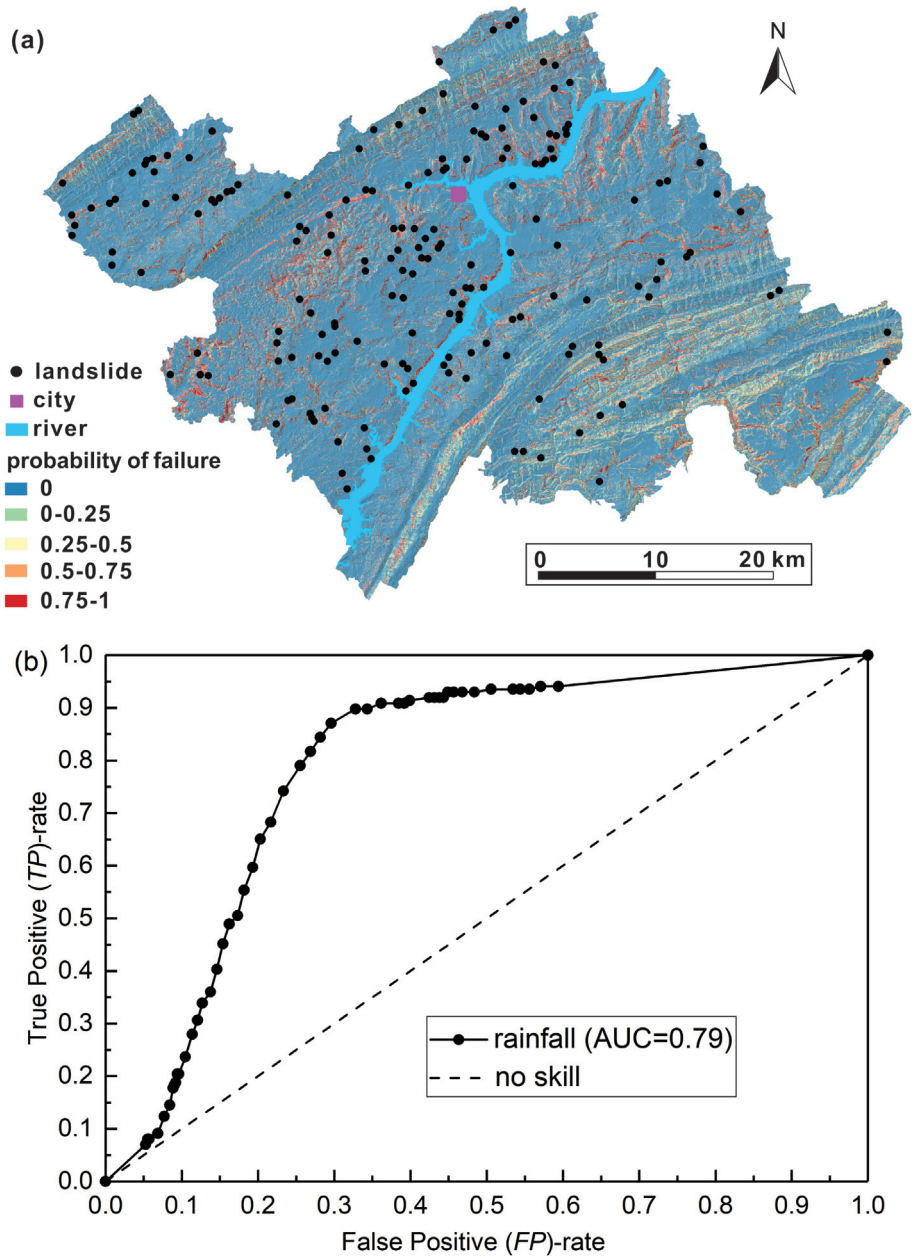

Fig. 6. Stability modelling results of the parameter calibration phase: (a) Probability of failure map obtained by using the best-fit parameters. (b) Analysis of area under the curve represented by *ROC*.

Table 4
Confusion matrix of the ROC-analysis when the *PoF* = 0.5 was selected as threshold.

Index	True positive (TP)	True negative (TN)	False positive (FP)	False negative (FN)	TP rate (TPR)	FP rate (FPR)	Accuracy (ACC)
Value	91	4189	811	95	0.489	0.162	0.664

Table 5
The multi-model ensemble utilized in this study for rainfall prediction, and the GCMs and RCMs included in the ensemble.

Ensembles No.	1	2	3	4
GCM	HadGEM2-ES	HadGEM2-ES	MPI-ESM-LR	MPI-ESM-MR
RCM	REMO2015	RegCM4	REMO2015	RegCM4

In order to obtain the predicted future scenarios P_a, the effective recharge ratio (*ERR*) is also necessary to determine q_a. The EasyBal software was used again to implement this goal following the procedure stated in section 3.2.2. In order to capture the trend of *ERR* change for the future scenarios, we used the precipitation time-series from the climate change model outputs during three different time periods: reference scenario (1995–2005), mid-21st century (2035–2045), and late 21st century (2075–2085). The projected daily precipitation data was derived from the mean value of 4-model ensemble (Table 5) to reduce the uncertainty in individual climate model outputs. According to existing literature (Ding et al., 2007; Huang et al., 2021), the magnitudes of increase for temperature in the two future scenarios were determined, whereas the daily evapotranspiration was calculated by the empirical formula (Hargreaves and Samani, 1982) built-in the software. Three *ERR* values (one for the reference scenario and two for the future scenarios) were obtained from the EasyBaL software during this step, and the ratios of future scenarios to the reference scenario (herein called R_{err}) were determined. Next, according to the *ERR* for the present condition (11.7%) obtained from the monitoring data (see section 3.2.2), the actual *ERR* values for the two future scenarios were determined by multiplying R_{err} to 11.7%.

For each scenario, there are two *ERR* values calculated. It is important to understand that the *ERR* results calculated from the climate change models are only used to reveal the relationship of *ERR*s between reference and future scenarios. The absolute values in this step do not make sense because the input precipitation and temperature time-series are not observed data.

After this step, the effective antecedent recharge (q_a) for future scenarios can be determined by using the P_a map, *CCF* and *ERR* values (Table 1).

3.4.2. Prediction of LULC change

The land change modeller (LCM) integrated into IDRISI Selva software was applied to analyse the land cover changes (Eastman, 2015). Generally, two LULC maps from different years are used to predict the LULC map in a third year. In this study, the LULC maps from 2000 and 2010 (CAS, 2021) were used as the inputs, which had the same spatial extent, reference system and land cover categories. The LCM follows a competitive land allocation procedure similar to the multi-objective land allocation algorithm (Eastman, 2009). Firstly, the LCM tool calculated the conversion between every-two land cover categories from 2000 to 2010 and obtained the conversion probability matrix. Based on this, the multi-layer perceptron neural network algorithm built in the LCM was used to generate the conversion potential maps from 2010 to the predictive year. Finally, the LCM allocated the land cover category to every pixel in the predictive year according to the conversion potential map and the quantity of the conversion (Khoi and Murayama, 2010).

During this stage, users also need to select reasonable spatial variables as the inputs. These variables are considered as the driving forces of the land cover changes in the area, and the observed changes may depend much on them. There is no agreement on the variables used for the drivers of LULC change so far, but three kinds of variables are widely applied in literature, namely climatic variables, physical accessibility variables and topographical variables (Khoi and Murayama, 2010; Molowny-Horas et al., 2015; Anand et al., 2018; Shu et al., 2019). Seven variables associated with these three categories were used in this study, and the ranges of these variables were larger than the ones used in Khoi et al. (2010) and Anand et al. (2018), but a littler smaller than those selected by (Molowny-Horas et al., 2015) and Shu et al. (2019). The details of these variables are as follows:

(i) Climatic variables: These kinds of variables have direct impacts on the land cover type because they can condition hydrological processes during the growth of plants. Two climatic variables were considered in this study. The average annual rainfall and temperature maps from 2000 to 2010 were generated from the spatial interpolation datasets of rainfall and temperature (CAS, 2021), respectively.

(ii) Physical accessibility variables: These variables can affect the accessibility of people to specific areas, and thus, different human activity intensities are caused. In our case, the distance to rivers and distance to roads were selected as the input variables.

(iii) Topographical variables: The environments vary with this type of variables, and local climatic regimes in mountainous areas can also be affected. The DEM, slope, and aspect are included in this category, and all of them have a resolution of 30 m. The slope and aspect maps were derived from the DEM through the "raster terrain analysis" tool in QGIS.

4. Results

4.1. Impacts of climate change

4.1.1. Future antecedent rainfall condition

The *CCF*s of antecedent rainfall (P_a) for future scenarios are shown in Fig. 7a and b. The *CCF* under the mid-21st century scenario is between 1.08 and 1.25, whereas the *CCF* for the late 21st century ranges from 1.31 to 1.63. Hence, it is evident that the future antecedent rainfall will increase over time. Higher values in the eastern region and lower values in the western region of the study area were observed for both rainfall changes. The *CCF* values in the west of the Yangtze River for the middle 21st century are less than 1.15 while those in the eastern areas are between 1.15 and 1.25. This indicates that there will be significant spatial variability in the magnitude of climate change even at a regional scale. Next, the P_a distribution for the two future scenarios were obtained by multiplying the *CCF* to the present P_a map. As seen in Fig. 7c and d, the P_a ranges from 6.55 mm/d to 7.68 mm/d in the middle of the 21st century, whereas the P_a is between 7.93 mm/d and 10.02 mm/d in the late 21st century.

The *ERR* values for different scenarios were derived from the EasyBal software by using the mean values of the precipitation data from the four climate change models (Table 5). Similar the *ERR* obtained from the observed data in the section 3.2.2, we still focused on the mean value of *ERR* in summer. As listed in Table 6, the *ERR*s obtained from the climate change model datasets were 1.4% for reference scenario, 2.9% for mid-21st century, and 1.6% for late 21st century, respectively. Hence, the trend of *ERR* changes for the future scenarios can be captured, which herein is expressed by the ratio to reference scenario: *ERR* for mid-21st century will be 2.07 times the reference scenario, whereas *ERR* for late 21st century will be 1.14 times. As the procedure stated in the section 3.4.1, based on this trend and the *ERR* for the reference scenario from the monitoring station (11.7%, see the section 3.2.2 for details), the actual *ERR* values for future scenarios were determined, namely 24.2% for mid-21st century, and 13.4% for late 21st century. These *ERR* values were considered as constant value for the entire region, and the effective antecedent recharge maps for the future scenarios were obtained by multiplying the *ERR* to the P_a map (Fig. 7e and f). Compared with the reference scenario, future scenarios have larger effective antecedent recharge with a maximum for the mid-21st century. These results may be explained, because the higher temperature time-series for the future scenarios in the EasyBal software caused higher evapotranspiration and smaller effective antecedent recharge. However, the overall trend of antecedent condition changes of rainfall is clear

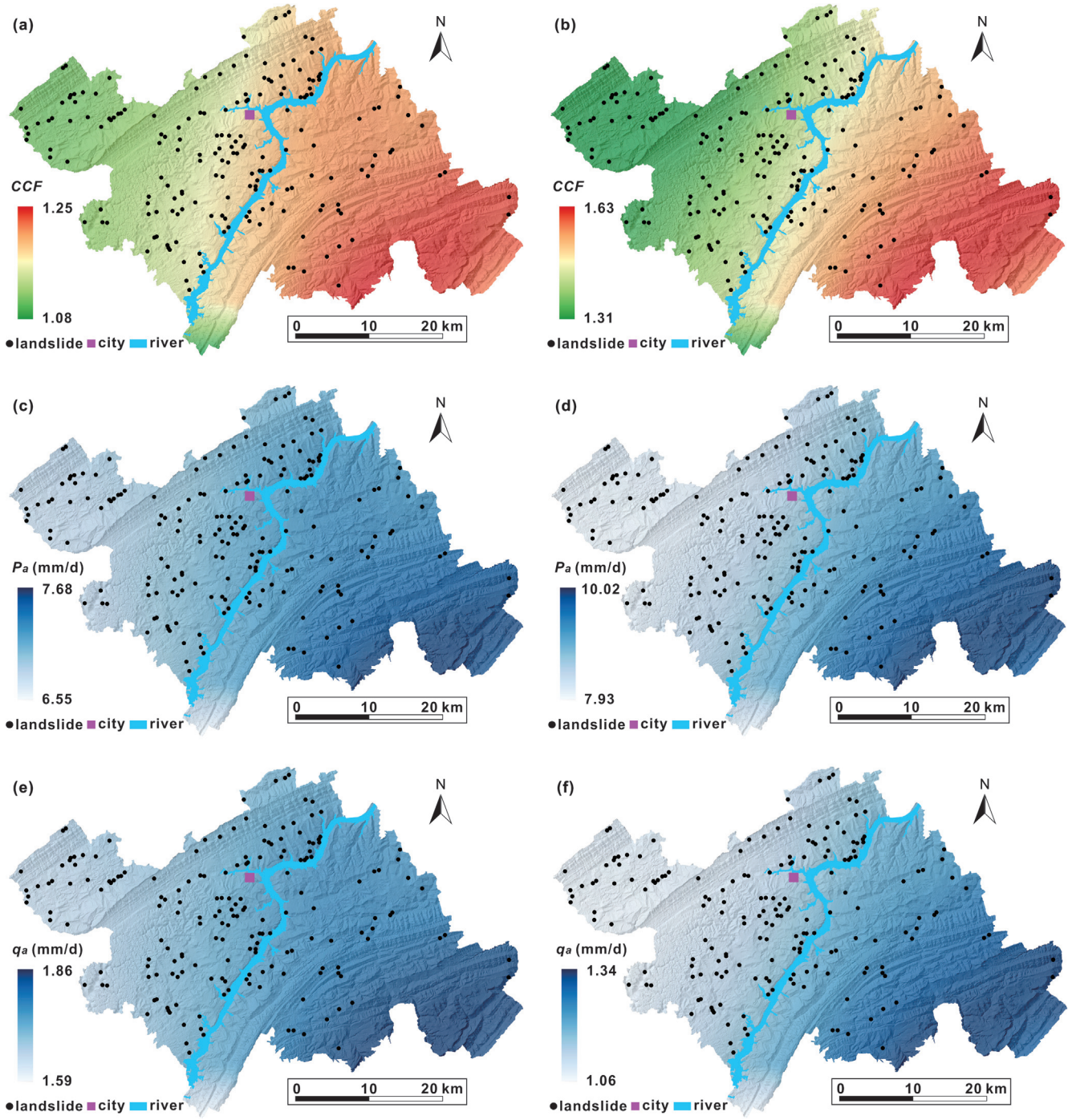

Fig. 7. Prediction results of future antecedent rainfall conditions in the study area: (a) *CCF* for mid-21st century, (b) *CCF* for late 21st century, (c) P_a distribution for mid-21st century, (d) P_a distribution for late 21st century, (e) q_a for mid-21st century, and (f) q_a for late 21st century.

Table 6
Results of the effective recharge ratios for different scenarios.

Scenario	Reference scenario	Mid 21th century	Late 21th century
ERR from climate change models	1.4%	2.9%	1.6%
Ratio to reference scenario	1	2.07	1.14
Actual value of *ERR*	11.7% (from the monitoring station)	24.2%	13.4%

in Wanzhou County, namely both P_a and q_a will increase in the future.

4.1.2. Future event rainfall

The *CCF*s of event rainfall for future scenarios with different return periods were obtained by modelling the frequency distribution for gridded precipitation data across the study area. The *CCF*s for the 100 years return period are shown in Fig. 8a and b. The event rainfall maps for the future scenarios were generated by multiplying the *CCF* to the P_e of the reference scenario (Fig. 8c and d). The event rainfall is also predicted to increase significantly

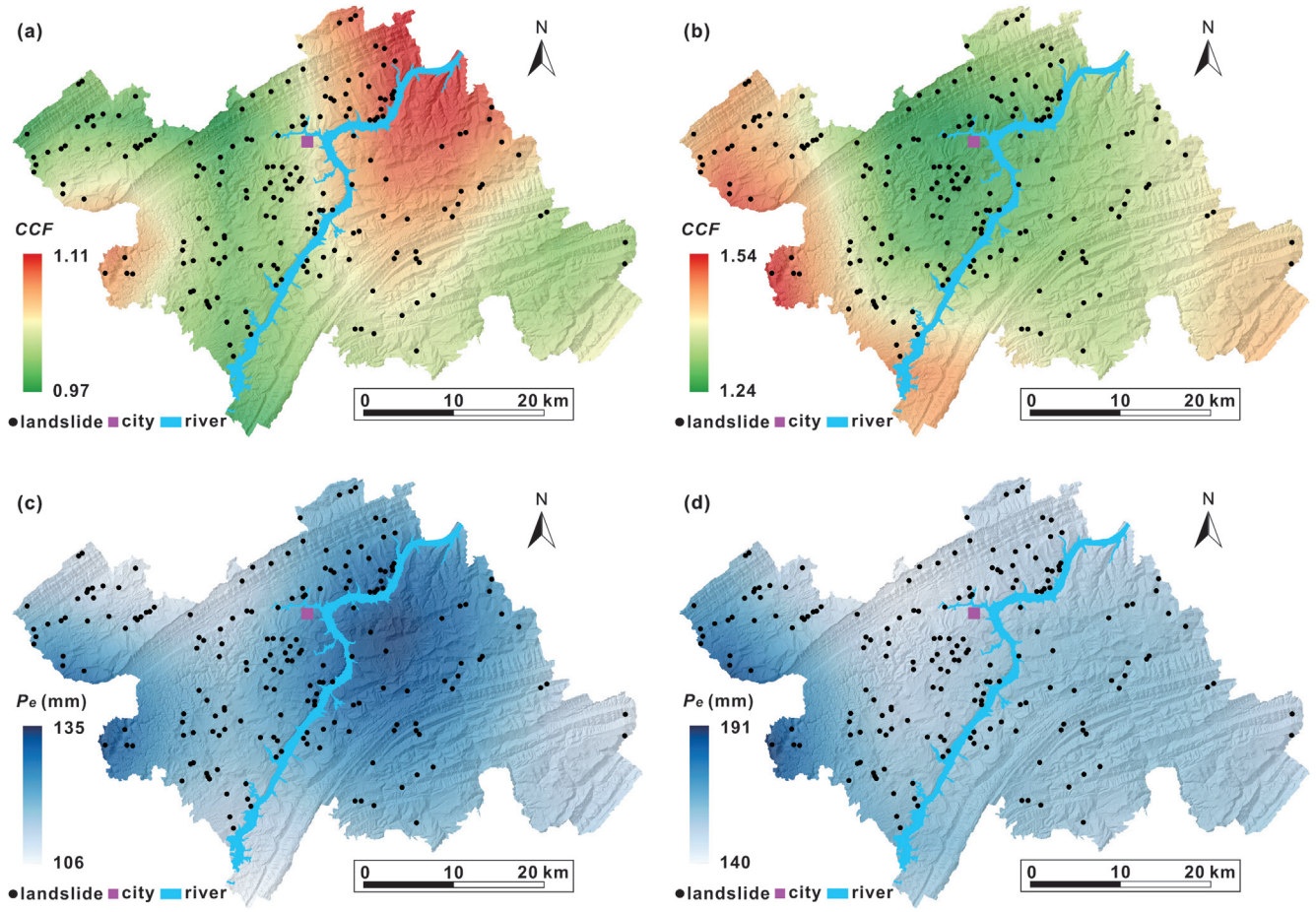

Fig. 8. Prediction results of future event rainfall for the return period of 100 years in the study area: (a) *CCF* for mid-21st century, (b) *CCF* for late 21st century, (c) P_e distribution for mid-21st century, and (d) P_e distribution for late 21st century.

in the future compared to that in the reference scenario. However, the late 21st century will have higher P_e than in the mid-21st century, which is different from the q_a condition for the future scenarios. Specifically, the increase of P_e in the late 21st century is even larger than that in the mid-21st century, which reveals that the extreme rainfall conditions will be important in the future.

4.1.3. Landslide susceptibility under future rainfall changes

All the landslide susceptibility maps under future climate changes were calculated by using the q_a and P_e rasters described in the previous sections. The LULC raster was the one for the reference scenario (year 2000). The probability of failure (*PoF*) map for the late 21st century with 100-year return period is shown in Fig. 9a. In order to visualize the change, the *PoF* difference at each cell was computed by subtracting the *PoF* of the reference scenario from this map. The results (Fig. 9b) show that the *PoF* in the Wanzhou region will generally increase (at most of the cells by 10% whereas at some points up to 65%) under the future rainfall scenarios. Only a minority of areas that are mainly located at the southeastern part have a *PoF* difference of 0, which indicates that the stability condition will not change in the future. The *PoF* values at most cells will increase up to 20% in the future. In conclusion, the stability condition in the study area will decrease because of the increasing q_a and P_e in the future.

The results from the cumulative distribution function (*CDF*) and the probability density function (*PDF*) of all the cells of each landslide susceptibility map also support the finding mentioned above. To highlight the trend of *CDF* and *PDF* among different scenarios, we plotted the *normalized CDF* and *PDF* vs *PoF*, respectively. The *normalized CDF* was determined by dividing the *CDF* for the future scenarios with the one for the reference scenario, whereas the *normalized PDF* was determined by subtracting the *PDF* for the reference scenario from the ones for the future scenarios. As shown in Fig. 9c, the *normalized CDF*s of different scenarios are less than 1 (except at *PoF* = 1). This indicates that the total number of cells with unstable conditions in the future scenarios is increasing. The *normalized PDF* curves (Fig. 9d) can better help us to understand this change. The future scenarios have more cells (*normalized PDF* greater than 0) at all *PoF* values, except 0, which means some cells drift from stable condition (*PoF* = 0) to unstable condition (*PoF* greater than 0) under the future climate change. In addition, another interesting finding is that the difference between mid and late 21st scenario are much smaller than that between reference and mid-21st scenario. This indicates that the impact of climate change may weaken in the far future compared with the near future. This can be explained by the opposite trends of q_a and P_e, where q_a will decrease from mid to late 21st century whereas the P_e will increase.

4.2. Impacts of LULC change

4.2.1. Future LULC scenarios

The results of LULC prediction implemented by the LCM are shown in Fig. 10. The result was first validated by the comparison between predicted and observed LULC maps in 2018 (Fig. 10a), and most categories have a good fitting, except the dense forest and

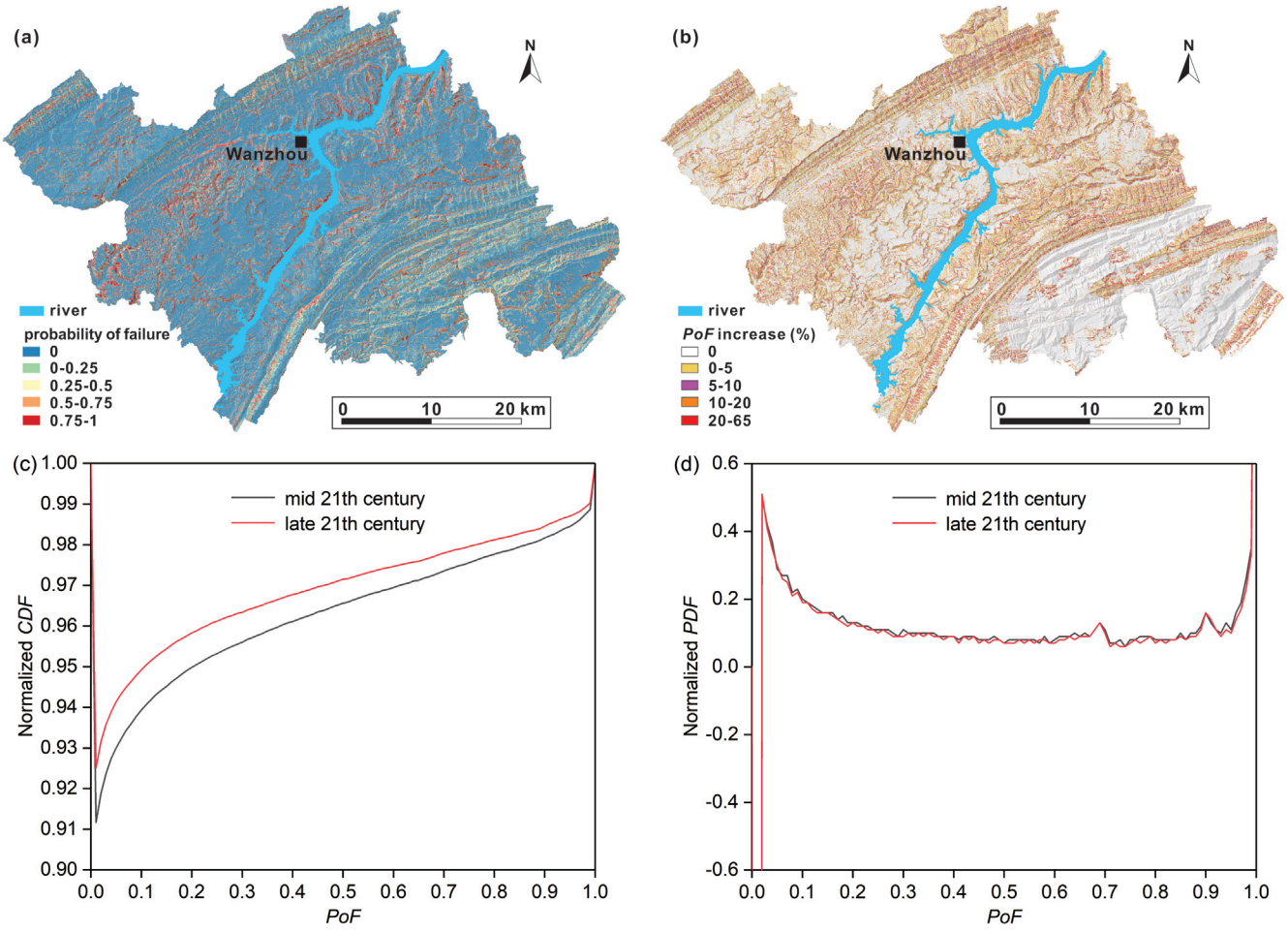

Fig. 9. Simulation results of landslide susceptibility for the future climate change scenarios: (a) *PoF* map for the late 21st century and the 100-years return period. (b) Difference of *PoF* between the future climate and the reference scenario. (c) Normalized *CDF* vs *PoF* in the resulting landslide susceptibility maps. (d) Normalized *PDF* vs *PoF*.

open forest. The dense forest has a lower predicted value than the observed value (–4.5%), while the open forest has a higher value than the observed one (+3.3%). This can be explained by the policy that the government encouraged extensive afforestation from the beginning of this century (Zhang et al., 2000; Li et al., 2018). Overall, the modelling accuracy is satisfactory.

During the next stage, the same inputs and model training process were used to predict the future LULC maps up to 2100 (Fig. 10b). The results show that the trends from 2000 to 2018 are mostly continuing in the future, namely, the increase of the dense forest and the decrease of the open forest. However, the change of dense forest is much larger than the one of open forest, so the total area of the forest will increase in the future. Additionally, some interesting changes were also observed. During the period from 2010 to 2100, the total area of agricultural land (paddy field and dry farmland) largely decreased by 161.7 km^2, accounting for 4.7% of the study area. A decrease of the area was also modelled for grassland, which decreased by 185 km^2. On the contrary, the area of shrubs increased to twice as much as before (98.8 km^2 in 2010 to 220.8 km^2 in 2100). Except for these categories, the changes of the other categories were of minor importance because their total areas were much smaller.

4.2.2. Landslide susceptibility under future LULC changes

The individual impact of LULC change towards different time periods was simulated by using the predicted LULC rasters and the rainfall rasters of the reference scenario. The example of the landslide susceptibility map for the late 21st century is shown in Fig. 11a, and the *PoF* difference between the reference scenario and this scenario is shown in Fig. 11b. It can be observed that *PoF* most cells in the study area will not change (*PoF* difference = 0) under the LULC changes. The *PoF* difference is negative at some cells which means that the stability condition in these areas will decrease in the future. On the contrary, the stability of cells will improve when the value of *PoF* difference is positive. The reason why different trends of *PoF* will occur is related to the transformations among vegetation categories from the present to the future. *PoF* will increase when the LULC changes from the category with higher root cohesion to that with smaller root cohesion (e.g., from forest to shrubs), and vice versa. In addition, the magnitude of these two trends are evidently different. In the zones which have worse stability conditions in the future (yellow and red region in Fig. 11b, the *PoF*s at most cells will increase by only a few percent compared with the reference. However, in the zones that will have better stability conditions (green and blue region in Fig. 11b), the change of *PoF*s from the reference to the future can reach 100%, namely from totally unstable (*PoF* = 1) to totally stable (*PoF* = 0).

To capture the overall trend of the stability condition under future LULC changes, the *normalized CDF* and *normalized PDF* curves were also analyzed. As shown in Fig. 11c and d, the two curves reveal different trends compared with that under climate change. The *normalized CDF* values are larger than 1, which shows that the number of cells from *PoF* = 0 to 0.99 in the future scenarios is greater than the cells of the reference scenario, and the number

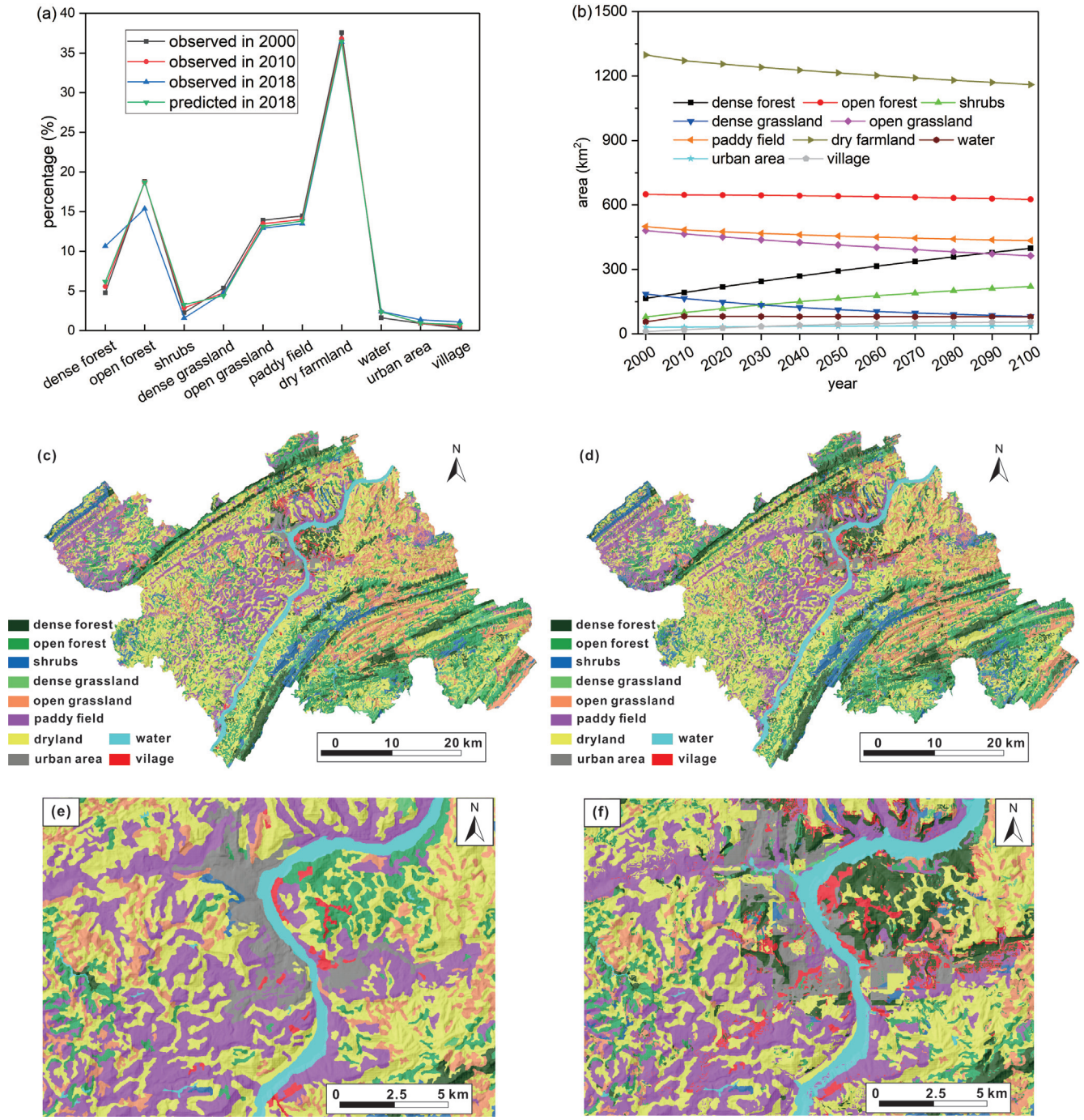

Fig. 10. Results of the LULC prediction: (a) Comparison between the predicted LULC map and the observed LULC map in 2018, where the LULC maps in 2000 and 2010 were used as the inputs. (b) Historic and future evolution of the LULC categories between 2000 and 2100 in the study area. (c) The predicted LULC map for mid-21st century (year 2040). (d) The predicted LULC map for the late 21st century (year 2080). The red rectangle represents the area shown in (e) and (f). (e) Zoomed area of the reference scenario (year 2000). (f) Zoomed area of the late 21st century (year 2080).

of cells between *PoF* = 0.99 to 1 in the future scenarios is smaller Regarding the *normalized PDF* curve, it can be roughly divided into two parts, with positive values for the *PoF* less than 0.4, and negative values for the *PoF* from 0.4 to 1. This reveals that the future scenarios have more stable cells and less unstable cells.

Hence, the overall stability condition in the Wanzhou region under the future LULC change will slightly improve. This is mainly because the major LULC change in the study area will be the increase of forest, which has higher root cohesion than other LULC categories. This confirms again the positive effect of afforestation on stabilizing slopes.

4.3. Comparison and evaluation of the impacts of future changes

During the final stage of the study, the combined impacts of LULC and climate changes were compared and evaluated for the two time periods. The *PoF* differences between the two future scenarios and the reference scenario are presented in Fig. 12. The negative values in the figure represent the decrease of *PoF* in the future scenarios compared with the reference scenarios, whereas positive values represent higher *PoF* in the future scenarios. As we can see, the stability condition of about half of the study area will not change in the future scenarios. The percentages of the zone with

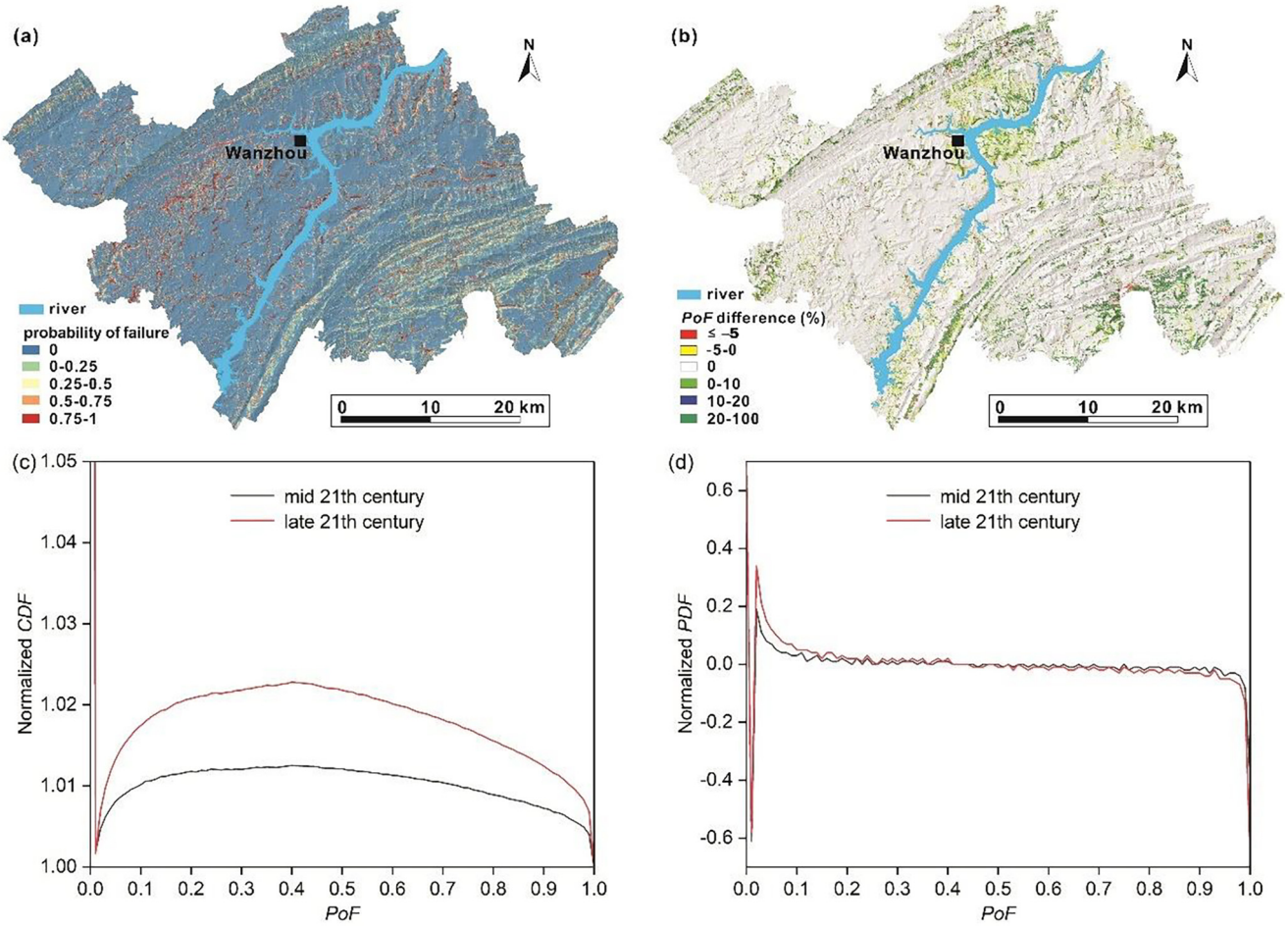

Fig. 11. Simulation results of landslide susceptibility for the future LULC change scenarios: (a) *PoF* map for the late 21st century (year 2080). (b) Difference of *PoF* between the reference scenario and the future LULC. (c) Normalized *CDF* vs *PoF* in the resulting landslide susceptibility maps. (d) Normalized *PDF* vs *PoF*.

the *PoF* difference of 0 in the two time periods are 54.6% (mid-21st century) and 51.7% (late 21st century), respectively. In the zones where the stability condition changes, the *PoF* at most cells will increase by 0–20%. In addition, only a small area will have lower *PoF* values in the future, which indicates a better stability condition in these areas. Another important finding from the figure is that the area with decreased *PoF* values in the late 21st century is larger compared with the one of the mid-21st century, especially in the southeastern part of the study area. This indicates that the overall stability in the late 21st century is better than that for the mid-21st century.

Next, we made statistics on the number of cells at each *PoF* difference value and plotted the *PDF* curves (Fig. 13a). The results support the conclusion stated above. Regarding the *PoF* difference from –0.8 to 0, the late 21st century has larger *PDF* values. This reveals that more cells in this scenario have decreased *PoF*. On the contrary, the mid-21st century has more cells when the *PoF* difference is between 0.2 and 0.8, which indicates that the *PoF* of more cells will increase in this scenario. Hence, it can be inferred that the overall stability conditions under the late 21st century will be better than the mid-21st century. This is mainly associated with the larger q_a value in the mid-21st century, because the rainfall input of antecedent condition has been proved to have a strong effect on the area with critical slope stability in the FSLAM modelling (Medina et al., 2020).

In order to compare and evaluate the stability condition under all the simulated future scenarios, a summarising graph was generated by showing the normalised *CDF* values for three different *PoF* values. As seen in Fig. 13b, it shows the difference of *CDF* by subtracting the *CDF* values of the reference scenario from the ones of the future scenarios. The selected three *PoF* values are 0.1, 0.5 and 0.9, respectively. The results confirm again the different impacts of LULC and climate changes. The difference of normalized *CDF* values reveals that the stabilizing effect related to LULC change is smaller than the destabilizing effect associated with the climate change. Hence, the overall stability condition in Wanzhou region will decrease in the future when the two changes are considered. However, the stability condition for the late 21st century will be slightly better than that for the mid-21st century. This also agrees well with the outcomes from Fig. 13a.

5. Discussion

In the following, three main aspects are discussed. First, the limitations associated with uncertainty will be explained. Then we compare our findings with the ones achieved by the most recent studies on the impacts of environmental changes on landslide activities. Finally, the potential scope of our future work will be described.

The origins and meanings of uncertainties that affect our modelling procedure and results are mainly related to the following aspects: (i) input parameter values and landslide inventory related to stability modelling; (ii) selection of variables in LCM used for LULC prediction; and (iii) the prediction of future rainfall by using

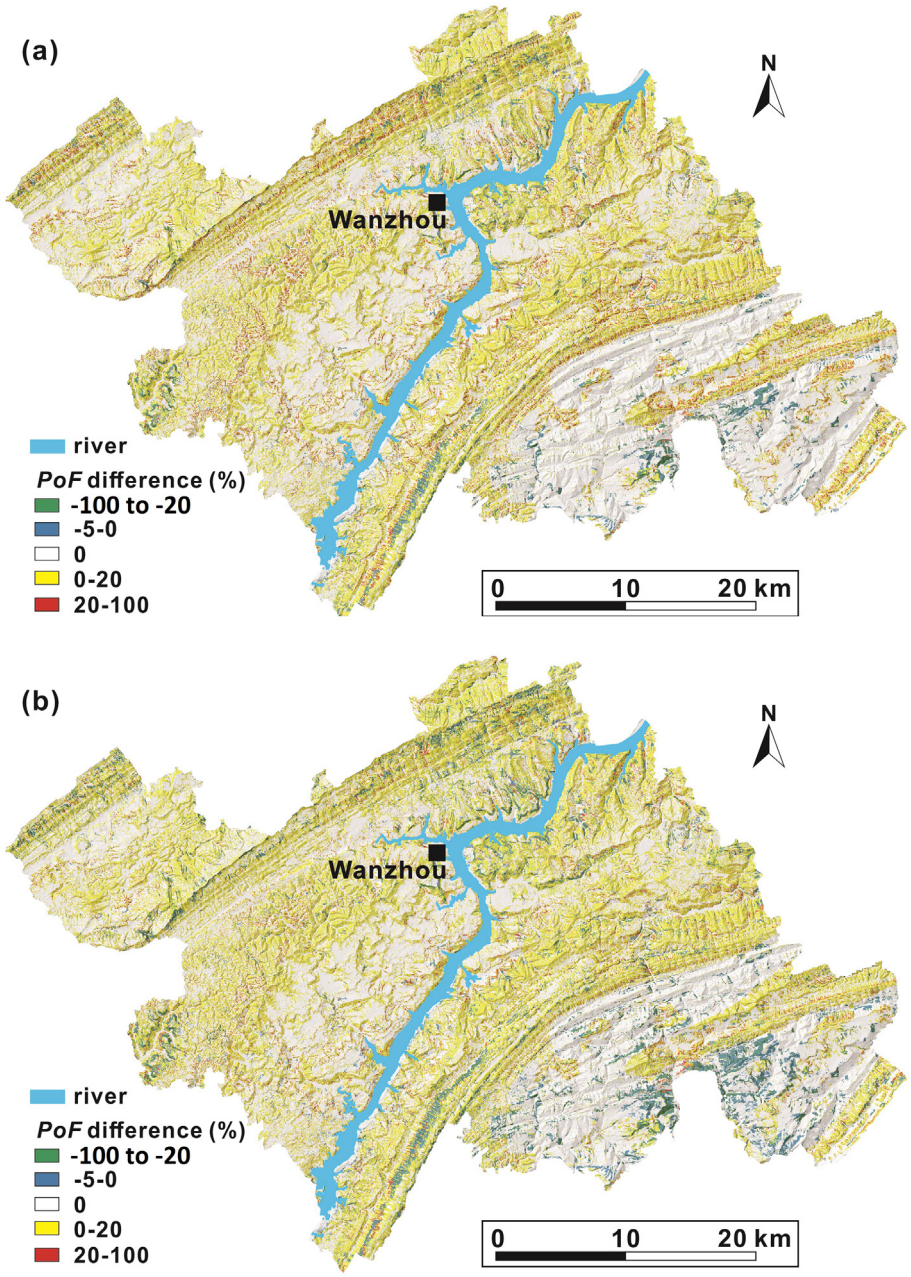

Fig. 12. The *PoF* difference between the future scenarios and the reference scenario: (a) for the mid-21st century, and (b) for the late 21st century.

frequency distribution model and multi-model ensemble. Regarding the first aspect, we only considered the two most important parameters (cohesion and internal friction angle) as stochastic inputs, although six soil properties were applied in the FSLAM model (Medina et al., 2020). Detailed analyses about the variability of spatial distribution of the input parameters are lacking, because it is a difficult task (Segoni et al., 2020). Another point that needs to be mentioned is the determination of landslide inventory. Considering some parameters (including root cohesion and rainfall) in the FSLAM model are dynamic over time, a landslide episode during a short period is important for parameter calibration. In some studies (e.g. Hürlimann et al. 2022), such a specific episode and related landslide inventory is available for the calibration step. However, this is not applicable for the case of Wanzhou County because the historical landslides in this region spread over several decades and the temporal distribution is rather dispersed (Xiao et al., 2019). Hence, we select the landslide inventory from 1995 to 2005 as an alternative, which reduces the temporal extent of landslides on one side, and on the other side, it reduces the effect of dynamic parameters during calibration. Given this point, landslide episodes triggered by future extreme storm events in Wanzhou region may be helpful to update these calibration parameters. Regarding the uncertainty that originated from the second aspect (predictive variables of LULC change), we only included some socioeconomic factors that act as drivers of LULC changes. Finally, only the distance to rivers and distance to roads were used as proxies. Although the uncertainties regarding points (i) and (ii) inherently exist in the input data and methodologies, our preliminary validation still confirmed the effectiveness of the modelling process: The accuracy of 0.79 expressed by the ROC curve indicated that the parameter calibration was accurately conducted for the stability modelling.

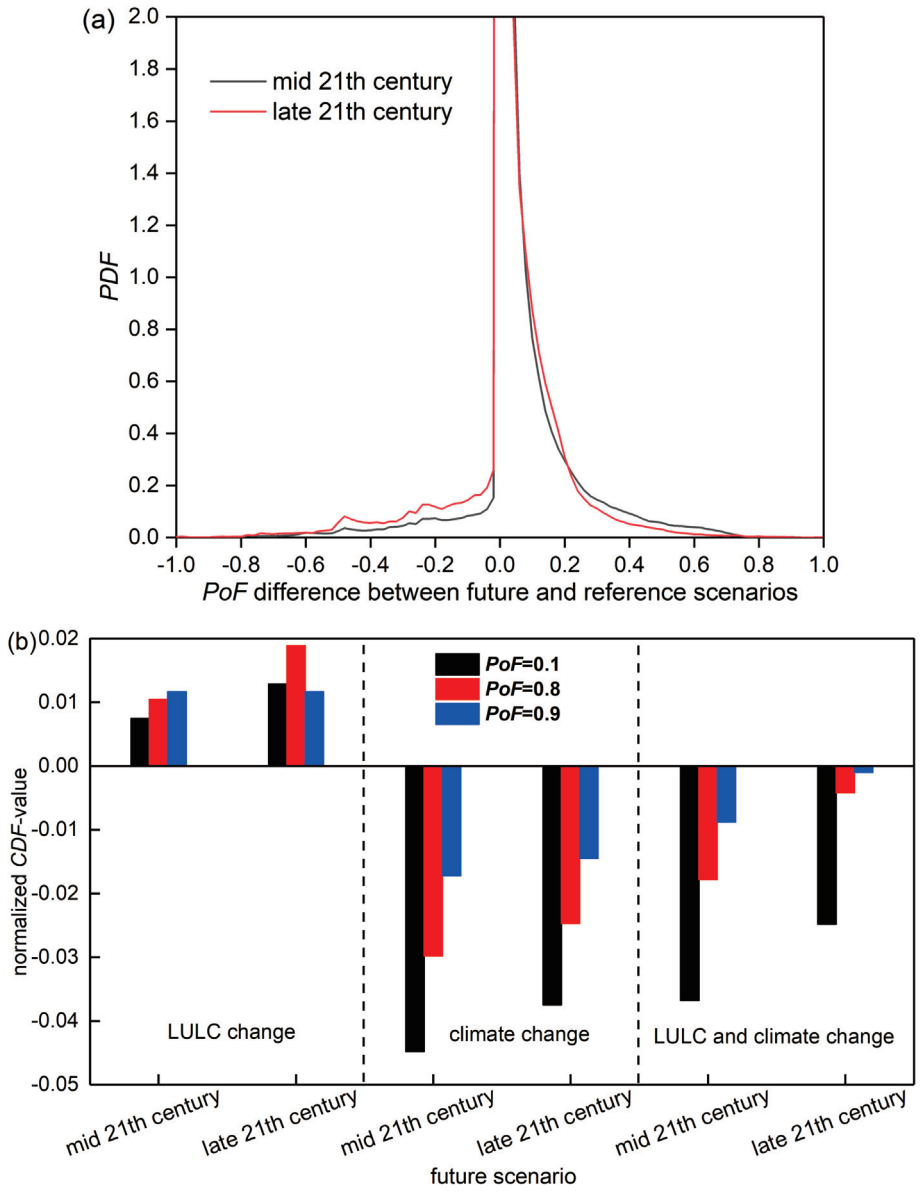

Fig. 13. Comparison and evaluation of the overall impacts of LULC and climate changes: (a) *PDF* curve of *PoF* difference between the future scenarios and the reference scenario. (b) Normalized *CDF* values for three different *PoF* values of all the calculated scenarios.

Regarding the third aspect, the prediction of climate change, many climatic and other environmental factors affect future slope stability conditions and we tried to include as much as possible. Here, two rainfall conditions (antecedent and event rainfall) and the potential increase of temperature were included for future changes, among which the temperature was used only for the estimation of ERR. Although adding more information into the model improves the predictive ability, the complexity and uncertainty will increase unavoidably (Crozier and Glade, 2012). There are multiply studies, which focus on the uncertainty analysis in terms of parameterizations and dataset resolution of climate models (Alvioli et al., 2018), and the role of bias correction have been reported (Ehret et al., 2012; Teutschbein and Seibert, 2012). In this study, the applied CMFD dataset may provide an important source of uncertainty at the beginning of the climate projections, because an assessment on gridded precipitation products found that the CMFD may underestimate extreme and accumulated rainfall (He et al., 2021). Besides, the uncertainty of future extreme rainfall can be also associated with the frequency distribution modelling, because the Gumbel distribution may underestimate the largest extreme rainfall amounts in comparison to other extreme value distributions (Koutsoyiannis, 2004). From the perspective of the previous statements, the predicted rainfall from climate models, especially event rainfall, is probably smaller when compared with station-derived indices. So, the stability condition under climate change may be even worse than the results simulated in this study. Another issue that should be paid attention to is the prediction combination from multiple climate models. In order to maintain the prediction results robust, we developed a multi-model ensemble including 4 RCMs and 3 GCMs. While the multi-model average appears to be useful to avoid uncertainty, our current analysis lacked the quantitative evaluation of model performance, which is always an operational challenge on this topic for researchers (Knutti et al., 2010).

This study analyses the evolution of landslide susceptibility under the combined effects of LULC and climate changes. Our results indicate that the climate change impacts on landslide activity in the study area are more important than the ones related to

LULC change. We try to understand this outcome through the comparison with other studies. On one hand, the future climate change scenarios imply the significant increase in landslide susceptibility, regardless of the considered scenario or the return period. This agrees well with previous studies (Ciervo et al., 2017; Alvioli et al., 2018) that applied different approaches but obtained similar general trends for various regions. On the other hand, the effect of LULC change on the stability condition in our study area is positive but relatively limited. Debatable findings have been reported in the literature regarding this point. The degree that the stability condition improves, may be rather large in a high mountain area (Hürlimann et al., 2022), while other researchers found that the specific transformation of LULC (e.g., deforestation) could also cause increase of regional landslide susceptibility (Reichenbach et al., 2014). This leads us to conclude that the impacts of future vegetation changes may be more dependent on local characteristics, and highly related to the socioeconomic background. For example, the abandonment of agriculture land and increase of forests were the most important LULC change in mountain areas of Europe during the twentieth century (MacDonald et al., 2000), while deforestation was more common in the Ecuadorian Andes during the same period due to increasing population pressure and economic development (Vanacker et al., 2003). Given that the magnitude of individual effects of both LULC and climate change is variable, the combined effect of the two changes on landslide susceptibility can vary in different test areas.

Last but not least, as future work we plan to include more aspects into the prediction of the LULC (e.g., more drivers like society and environment variables, the effect of wildfires) and climate changes (e.g., analysis of the balance of rainfall and snow, combined factor of evapotranspiration affected by vegetation, rainfall and temperature). Future results from global climate models will also provide more robust input data and surely reduce the variability and uncertainties of data. In addition, it would be highly interesting to employ the current procedure in other territories to test the effects of environmental changes, which will certainly reveal better insights on this topic.

6. Conclusions

The present study explored the individual and combined effects of LULC and climate changes on slope stability of Wanzhou County in China. A total of six future scenarios were defined and regional shallow landslide susceptibility under each scenario was simulated by applying a physical model. The results under each scenario were compared with the ones obtained for the reference scenario.

The results of the climate change analysis highlighted considerable changes of both antecedent conditions and event rainfall in the study area up to the late 21st century. The antecedent rainfall in summer will increase between 8% and 63%, whereas the event rainfall will increase by up to 54% with a return period of 100 years. In addition, both rainfall conditions will increase from the mid-21st century to the late 21st century. However, the effective recharge ratio (*ERR*) of the mid-21st time period will be evidently higher than that of the late 21st time period, which causes the antecedent effective recharge to show an opposite trend compared with an antecedent rainfall condition.

The results of the LULC prediction showed that the area of forests will increase while the agriculture land will decrease evidently in the future. In addition, the increase of shrubs and decrease of grassland were also observed are relatively minor in magnitude.

The LULC changes will improve the slope stability in the region due to higher root cohesion of forest and shrubs. On the contrary, the overall stability condition will decrease when focusing on the individual impact of climate change. The simulations and comparisons of landslide susceptibility for different scenarios found that the negative impact of climate change on landslide susceptibility is greater than the stabilizing effect of LULC change, thus the stability condition in the study area will decrease in the future.

This study is one of the first attempts across Asia to quantify and assess the impacts of LULC and climate change on regional landslide susceptibility. Our results are helpful to improve the understanding of magnitude and consequences of future environmental changes, and to support decision-makers with this knowledge for landslide risk mitigation.

CRediT authorship contribution statement

Zizheng Guo: Data curation; Formal analysis; Investigation; Methodology; Software; Validation; Visualization; Writing - original draft. **Joaquin Vicente Ferrer:** Data curation; Formal analysis; Methodology; Software; Validation; Writing - original draft. **Marcel Hürlimann:** Conceptualization; Funding acquisition; Methodology; Project administration; Supervision; Writing - review & editing. **Vicente Medina:** Conceptualization; Methodology; Supervision; Writing - review & editing. **Carol Puig-Polo:** Supervision; Writing - review & editing. **Kunlong Yin:** Data curation; Funding acquisition; Resources; Supervision. **Da Huang:** Data curation; Funding acquisition; Resources; Supervision; Writing - review & editing.

Declaration of Competing Interest

The authors declare that they have no known competing financial interests or personal relationships that could have appeared to influence the work reported in this paper.

Acknowledgements

This study was funded by the National Natural Science Foundation of China (Grant No. 41972297), Talents in Hebei Provincial Education Office (Grant No. SLRC2019027), Natural Science Foundation of Hebei Province (Grant No. D2022202005), and the Spanish national project EROSLOP (Grant No. PID2019-104266RB-I00/AEI/10.13039/501100011033). Zizheng Guo acknowledges the financial support of China Scholarship Council for his research at UPC BarcelonaTECH. Joaquin Ferrer acknowledges support from the Erasmus + Joint Master Degree Programme Flood Risk Management funded by the European Commission and run by IHE Delft, No. 2018-1514. The China Meteorological Forcing Dataset is provided by the National Tibetan Plateau Data Center (https://data.tpdc.ac.cn/).

References

Al-Najjar, H.A.H., Pradhan, B., Sarkar, R., Beydoun, G., Alamri, A., 2021. A new integrated approach for landslide data balancing and spatial prediction based on generative adversarial networks (GAN). Remote Sens. 13, 4011. https://doi.org/10.3390/rs13194011.

Althuwaynee, O.F., Pradhan, B., 2017. Semi-quantitative landslide risk assessment using GIS-based exposure analysis in Kuala Lumpur City. Geomatics. Nat. Hazards Risk 8, 706–732. https://doi.org/10.1080/19475705.2016.1255670.

Alvioli, M., Melillo, M., Guzzetti, F., Rossi, M., Palazzi, E., von Hardenberg, J., Brunetti, M.T., Peruccacci, S., 2018. Implications of climate change on landslide hazard in Central Italy. Sci. Total Environ. 630, 1528–1543. https://doi.org/10.1016/j.scitotenv.2018.02.315.

Anand, J., Gosain, A.K., Khosa, R., 2018. Prediction of land use changes based on Land Change Modeler and attribution of changes in the water balance of Ganga basin to land use change using the SWAT model. Sci. Total Environ. 644, 503–519. https://doi.org/10.1016/j.scitotenv.2018.07.017.

Berg, P., Moseley, C., Haerter, J.O., 2013. Strong increase in convective precipitation in response to higher temperatures. Nat. Geosci. 6, 181–185. https://doi.org/10.1038/ngeo1731.

Bernardie, S., Vandromme, R., Thiery, Y., Houet, T., Grémont, M., Masson, F., Grandjean, G., Bouroullec, I., 2021. Modelling landslide hazards under global changes: the case of a Pyrenean valley. Nat. Hazards Earth Syst. Sci. 21, 147–169. https://doi.org/10.5194/nhess-21-147-2021.

Bicocchi, G., Tofani, V., D'Ambrosio, M., Tacconi-Stefanelli, C., Vannocci, P., Casagli, N., Lavorini, G., Trevisani, M., Catani, F., 2019. Geotechnical and hydrological characterization of hillslope deposits for regional landslide prediction modeling. Bull. Eng. Geol. Environ. 78, 4875–4891. https://doi.org/10.1007/s10064-018-01449-z.

Camilo, D.C., Lombardo, L., Mai, P.M., Dou, J., Huser, R., 2017. Handling high predictor dimensionality in slope-unit-based landslide susceptibility models through LASSO-penalized Generalized Linear Model. Environ. Model. Softw. 97, 145–156. https://doi.org/10.1016/j.envsoft.2017.08.003.

CAS, 2021. Resource and Environment Science and Data Center of Chinese Academy of Sciences. http://www.resdc.cn/ (accessed on 20 November 2021).

Chen, L., Guo, Z., Yin, K., Pikha Shrestha, D., Jin, S., 2019. The influence of land use and land cover change on landslide susceptibility: A case study in Zhushan Town, Xuan'en County (Hubei, China). Nat. Hazards Earth Syst. Sci. 19, 2207–2228. https://doi.org/10.5194/nhess-19-2207-2019.

Christensen, J.H., Kjellström, E., Giorgi, F., Lenderink, G., Rummukainen, M., 2010. Weight assignment in regional climate models. Clim. Res. 44, 179–194. https://doi.org/10.3354/cr00916.

Ciervo, F., Rianna, G., Mercogliano, P., Papa, M.N., 2017. Effects of climate change on shallow landslides in a small coastal catchment in southern Italy. Landslides 14, 1043–1055. https://doi.org/10.1007/s10346-016-0743-1.

Collison, A., Wade, S., Griffiths, J., Dehn, M., 2000. Modelling the impact of predicted climate change on landslide frequency and magnitude in SE England. Eng. Geol. 55, 205–218. https://doi.org/10.1016/S0013-7952(99)00121-0.

Crozier, M.J.J., 2010. Deciphering the effect of climate change on landslide activity: A review. Geomorphology 124, 260–267. https://doi.org/10.1016/j.geomorph.2010.04.009.

Crozier, M.J., Glade, T., 2012. A Review of Scale Dependency in Landslide Hazard and Risk Analysis, in: Landslide Hazard and Risk. Doi: 10.1002/9780470012659.ch3.

Cruden, D.M., Varnes, D.J., 1996. Landslide types and processes. In: Turner, A.K., Schuster, R.L. (Eds.), Landslides: Investigation and Mitigation. Transportation Research Board, Washington DC, pp. 36–75.

Delignette-Muller, M.L., Dutang, C., 2015. fitdistrplus: An R package for fitting distributions. J. Stat. Softw. 64, 1–34 https://doi.org/10.18637/jss.v064.i04.

Dikshit, A., Sarkar, R., Pradhan, B., Acharya, S., Alamri, A.M., 2020. Spatial landslide risk assessment at Phuentsholing. Bhutan. Geosci. 10, 131. https://doi.org/10.3390/geosciences10040131.

Ding, Y., Ren, G., Zhao, Z., Xu, Y., Luo, Y., Li, Q., Zhang, J., 2007. Detection, causes and projection of climate change over China: An overview of recent progress. Adv. Atmos. Sci. 24, 954–971. https://doi.org/10.1007/s00376-007-0954-4.

Eastman, J.R., 2009. IDRISI Taiga. Guide to GIS and Remote Processing. Clark University, Worcester, MA, USA, pp. 234–256.

Eastman, J.R., 2015. TerrSet: Geospatial Monitoring and Modeling Software. Clark Las 53.

Ehret, U., Zehe, E., Wulfmeyer, V., Warrach-Sagi, K., Liebert, J., 2012. HESS Opinions "should we apply bias correction to global and regional climate model data? Hydrol. Earth Syst. Sci. 16, 3391–3404. https://doi.org/10.5194/hess-16-3391-2012.

Fanelli, G., Salciarini, D., Tamagnini, C., 2016. Reliable soil property maps over large areas: a case study in central Italy. J. Environ. Eng. Geosci. XXII 37–52. https://doi.org/10.2113/eeg-1709.

Fang, B., Chen, G., Pan, L., Kou, R., Wang, L., 2021. GAN-Based Siamese Framework for Landslide Inventory Mapping Using Bi-Temporal Optical Remote Sensing Images. IEEE Geosci. Remote Sens. Lett. 18, 391–395. https://doi.org/10.1109/LGRS.2020.2979693.

Fell, R., Corominas, J., Bonnard, C., Cascini, L., Leroi, E., Savage, W.Z., and on behalf of the JTC-1 Joint Technical Committee on Landslides and Engineered Slopes, 2008. Guidelines for landslide susceptibility, hazard and risk zoning for land use planning. Eng. Geol. 102, 99–111.

Ferrer, J., Guo, Z., Medina, V., Puig-Polo, C., Hürlimann, M., 2022. A Framework to Project Future Rainfall Scenarios: An Application to Shallow Landslide-Triggering Summer Rainfall in Wanzhou County China. Water 14, 873. https://doi.org/10.3390/w14060873.

Fischer, M., Rust, H.W., Ulbrich, U., 2018. Seasonal cycle in German daily precipitation extremes. Meteorol. Zeitschrift 27, 3–13. https://doi.org/10.1127/metz/2017/0845.

Freychet, N., Hsu, H.H., Chou, C., Wu, C.H., 2015. Asian summer monsoon in CMIP5 projections: A link between the change in extreme precipitation and monsoon dynamics. J. Clim. https://doi.org/10.1175/JCLI-D-14-00449.1.

Gao, X., Shi, Y., Han, Z., Wang, M., Wu, J., Zhang, D., Xu, Y., Giorgi, F., 2017. Performance of RegCM4 over major river basins in China. Adv. Atmos. Sci. 34, 441–455. https://doi.org/10.1007/s00376-016-6179-7.

Gariano, S.L., Rianna, G., Petrucci, O., Guzzetti, F., 2017. Assessing future changes in the occurrence of rainfall-induced landslides at a regional scale. Sci. Total Environ. 596–597, 417–426. Doi: 10.1016/j.scitotenv.2017.03.103.

Gariano, S.L., Guzzetti, F., 2016. Landslides in a changing climate. Earth-Science Rev. 162, 227–252. https://doi.org/10.1016/j.earscirev.2016.08.011.

Geospatial Data Cloud, 2021. ASTER GDEM data with 30 m. http://www.gscloud.cn/home (accessed 20 June 2021).

Grandjean, G., Thomas, L., Bernardie, S., Puissant, A., Malet, J.P., Houet, T., Bourrier, F., Fort, M., 2018. A Novel multi-risk assessment web-tool for evaluating future impacts of global change in Mountainous Areas. Climate 6(4), 92. https://doi.org/10.3390/cli6040092.

Gu, H., Yu, Z., Yang, C., Ju, Q., 2018. Projected changes in hydrological extremes in the Yangtze River basin with an ensemble of regional climate simulations. Water 10(9), 1279. https://doi.org/10.3390/W10091279.

Guo, C., Xu, Q., Dong, X., Li, W., Zhao, K., Lu, H., Ju, Y., 2021. Geohazard Recognition and Inventory Mapping Using Airborne LiDAR Data in Complex Mountainous Areas. J. Earth Sci. 32, 1079–1091. https://doi.org/10.1007/s12583-021-1467-2.

Guo, Z., Yin, K., Huang, F., Fu, S., Zhang, W., 2019. Evaluation of landslide susceptibility based on landslide classification and weighted frequency ratio model. Chinese in Chinese J. Rock Mech. Eng. 38, 287–300. https://doi.org/10.13722/j.cnki.jrme.2018.0838.

Guo, Z., Chen, L., Gui, L., Du, J., Yin, K., Do, H.M., 2020. Landslide displacement prediction based on variational mode decomposition and WA-GWO-BP model. Landslides 17, 567–583. https://doi.org/10.1007/s10346-019-01314-4.

Hargreaves, G.H., Samani, Z.A., 1982. Estimating potential evapotranspiration. J. Irrig. Drain. Div. - ASCE 108, 225–230. https://doi.org/10.1061/taceat.0008673.

He, J., Yang, K., Tang, W., Lu, H., Qin, J., Chen, Y., Li, X., 2020. The first high-resolution meteorological forcing dataset for land process studies over China. Sci. Data 7, 1–11. https://doi.org/10.1038/s41597-020-0369-y.

He, Q., Yang, J., Chen, H., Liu, J., Ji, Q., Wang, Y., Tang, F., 2021. Evaluation of extreme precipitation based on three long-term gridded products over the qinghai-tibet plateau. Remote Sens. 13, 3010. https://doi.org/10.3390/rs13153010.

Hertig, E., Jacobeit, J., 2008. Downscaling future climate change: Temperature scenarios for the Mediterranean area. Glob. Planet. Change 63, 127–131. https://doi.org/10.1016/j.gloplacha.2007.09.003.

Huang, Y., Xiao, W., Hou, B., Zhou, Y., Hou, G., Yi, L., Cui, H., 2021. Hydrological projections in the upper reaches of the Yangtze River Basin from 2020 to 2050. Sci. Rep. 11, 9720. https://doi.org/10.1038/s41598-021-88135-5.

Huang, F., Yin, K., Huang, J., Gui, L., Wang, P., 2017. Landslide susceptibility mapping based on self-organizing-map network and extreme learning machine. Eng. Geol. 223, 11–22. https://doi.org/10.1016/j.enggeo.2017.04.013.

Hungr, O., Leroueil, S., Picarelli, L., 2014. The Varnes classification of landslide types, an update. Landslides 11, 167–194. https://doi.org/10.1007/s10346-013-0436-y.

Hürlimann, M., Guo, Z., Puig-Polo, C., Medina, V., 2022. Impacts of future climate and land cover changes on landslide susceptibility: regional scale modelling in the Val d'Aran region (Pyrenees, Spain). Landslides 19, 99–118. https://doi.org/10.1007/s10346-021-01775-6.

Ilyina, T., Six, K.D., Segschneider, J., Maier-Reimer, E., Li, H., Núñez-Riboni, I., 2013. Global ocean biogeochemistry model HAMOCC: Model architecture and performance as component of the MPI-Earth system model in different CMIP5 experimental realizations. J. Adv. Model. Earth Syst. 5, 287–315. https://doi.org/10.1029/2012MS000178.

Geotechdata, 2021. Geotechdata. URL https://www.geotechdata.info/parameter. (accessed 11 May 2021).

IPCC, 2014. Climate Change 2014: Synthesis Report Contribution of Working Groups I, II and III to the Fifth Assessment Report of the Intergovernmental Panel on Climate Change, in: R.Pachauri, L. Meyer (Ed.), Climate Change 2014: Synthesis Report. Gevena, Switzerland, pp. 151.

IUSS Working Group WRB, 2014. World reference base for soil resources 2014. International soil classification system for naming soils and creating legends for soil maps, World Soil Resources Reports No. 106. https://doi.org/10.1017/S0014479706394902.

Jones, C.D., Hughes, J.K., Bellouin, N., Hardiman, S.C., Jones, G.S., Knight, J., Liddicoat, S., O'Connor, F.M., Andres, R.J., Bell, C., Boo, K.O., Bozzo, A., Butchart, N., Cadule, P., Corbin, K.D., Doutriaux-Boucher, M., Friedlingstein, P., Gornall, J., Gray, L., Halloran, P.R., Hurtt, G., Ingram, W.J., Lamarque, J.F., Law, R.M., Meinshausen, M., Osprey, S., Palin, E.J., Parsons Chini, L., Raddatz, T., Sanderson, M.G., Sellar, A. A., Schurer, A., Valdes, P., Wood, N., Woodward, S., Yoshioka, M., Zerroukat, M., 2011. The HadGEM2-ES implementation of CMIP5 centennial simulations. Geosci. Model Dev. 4, 543–570. https://doi.org/10.5194/gmd-4-543-2011.

Kharin, V.V., Zwiers, F.W., Zhang, X., Wehner, M., 2013. Changes in temperature and precipitation extremes in the CMIP5 ensemble. Clim. Change 119, 345–357. https://doi.org/10.1007/s10584-013-0705-8.

Khoi, D.D., Murayama, Y., 2010. Forecasting areas vulnerable to forest conversion in the tam Dao National Park region. Vietnam. Remote Sens. 2, 1249–1272. https://doi.org/10.3390/rs2051249.

Kirschbaum, D., Kapnick, S.B., Stanley, T., Pascale, S., 2020. Changes in Extreme Precipitation and Landslides Over High Mountain Asia. Geophys. Res. Lett. 47, e2019GL085347. Doi: 10.1029/2019GL085347.

Knutti, R., Furrer, R., Tebaldi, C., Cermak, J., Meehl, G.A., 2010. Challenges in combining projections from multiple climate models. J. Clim. 23, 2739–2758. https://doi.org/10.1175/2009JCLI3361.1.

Kotlarski, S., Keuler, K., Christensen, O.B., Colette, A., Déqué, M., Gobiet, A., Goergen, K., Jacob, D., Lüthi, D., Van Meijgaard, E., Nikulin, G., Schär, C., Teichmann, C., Vautard, R., Warrach-Sagi, K., Wulfmeyer, V., 2014. Regional climate modeling on European scales: A joint standard evaluation of the EURO-CORDEX RCM ensemble. Geosci. Model Dev. 7, 1297–1333. https://doi.org/10.5194/gmd-7-1297-2014.

Koutsoyiannis, D., 2004. Statistics of extremes and estimation of extreme rainfall: I. Theoretical investigation. Hydrol. Sci. J. 49, 575–590. https://doi.org/10.1623/hysj.49.4.575.54430.

Lan, H., Wang, D., He, S., Fang, Y., Chen, W., Zhao, P., Qi, Y., 2020. Experimental study on the effects of tree planting on slope stability. Landslides 17, 1021–1035. https://doi.org/10.1007/s10346-020-01348-z.

Li, Q., Huang, D., Pei, S., Qiao, J., Wang, M., 2021. Using Physical Model Experiments for Hazards Assessment of Rainfall-Induced Debris Landslides. J. Earth Sci. 32, 1113–1128. https://doi.org/10.1007/s12583-020-1398-3.

Li, Y., Piao, S., Li, L.Z.X., Chen, A., Wang, X., Ciais, P., Huang, L., Lian, X., Peng, S., Zeng, Z., Wang, K., Zhou, L., 2018. Divergent hydrological response to large-scale afforestation and vegetation greening in China. Sci. Adv. 4, eaar4182. https://doi.org/10.1126/sciadv.aar4182.

Liu, Y.i., Yin, K., Chen, L., Wang, W., Liu, Y., 2016. A community-based disaster risk reduction system in Wanzhou, China. Int. J. Disaster Risk Reduct. 19, 379–389. https://doi.org/10.1016/j.ijdrr.2016.09.009.

MacDonald, D., Crabtree, J.R., Wiesinger, G., Dax, T., Stamou, N., Fleury, P., Gutierrez Lazpita, J., Gibon, A., 2000. Agricultural abandonment in mountain areas of Europe: Environmental consequences and policy response. J. Environ. Manage. 59, 47–69. https://doi.org/10.1006/jema.1999.0335.

Medina, V., Hürlimann, M., Guo, Z., Lloret, A., Vaunat, J., 2020. Fast physically-based model for rainfall-induced landslide susceptibility assessment at regional scale. CATENA 201, 105213. https://doi.org/10.1016/j.catena.2021.105213.

Molowny-Horas, R., Basnou, C., Pino, J., 2015. A multivariate fractional regression approach to modeling land use and cover dynamics in a Mediterranean landscape. Comput. Environ. Urban Syst. 54, 47–55. https://doi.org/10.1016/j.compenvurbsys.2015.06.001.

Moss, R., Babiker, M., Brinkman, S., Calvo, E., Carter, T., Edmonds, J., Elgizouli, I., Emori, S., Erda, L., Hibbard, K., Jones, R., Kainuma, M., Kelleher, J., Lamarque, J.F., Manning, M., Matthews, B., Meehl, J., Meyer, L., Mitchell, J., Nakicenovic, N., O'Neill, B., Pichs, R., Riahi, K., Rose, S., Runci, P., Stouffer, R., Vuuren, D. van, Weyant, J., Wilbanks, T., Ypersele, J.P. van, Zurek, M., 2008. Towards New Scenarios for Analysis of Emissions, Climate Change, Impacts and Response Strategies, IPCC Expert Meeting Report.

Palmer, T., Stevens, B., 2019. The scientific challenge of understanding and estimating climate change. Proc. Natl. Acad. Sci. U. S. A. 116, 24390–24395. https://doi.org/10.1073/pnas.1906691116.

Patton, A.I., Rathburn, S.L., Capps, D.M., 2019. Landslide response to climate change in permafrost regions. Geomorphology 340, 116–128. https://doi.org/10.1016/j.geomorph.2019.04.029.

Qin, P., Xie, Z., Zou, J., Liu, S., Chen, S., 2021. Future Precipitation Extremes in China under Climate Change and Their Physical Quantification Based on a Regional Climate Model and CMIP5 Model Simulations. Adv. Atmos. Sci. 38 (3), 460–479. https://doi.org/10.1007/s00376-020-0141-4.

Rafiei Sardooi, E., Azareh, A., Mesbahzadeh, T., Soleimani Sardoo, F., Parteli, E.J.R., Pradhan, B., 2021. A hybrid model using data mining and multi-criteria decision-making methods for landslide risk mapping at Golestan Province. Iran. Environ. Earth Sci. 80, 487. https://doi.org/10.1007/s12665-021-09788-z.

Reichenbach, P., Busca, C., Mondini, A.C., Rossi, M., 2014. The Influence of Land Use Change on Landslide Susceptibility Zonation: The Briga Catchment Test Site (Messina, Italy). Environ. Manage. 54, 1372–1384. https://doi.org/10.1007/s00267-014-0357-0.

Roura-Pascual, N., Pons, P., Etienne, M., Lambert, B., 2005. Transformation of a rural landscape in the Eastern Pyrenees between 1953 and 2000. Mt. Res. Dev. 25, 252–261. https://doi.org/10.1659/0276-4741(2005)025[0252:TOARLI]2.0.CO;2.

Runyan, C.W., D'Odorico, P., 2014. Bistable dynamics between forest removal and landslide occurrence. Water Resour. Res. 50, 1112–1130. https://doi.org/10.1002/2013WR014819.

Rust, H.W., Maraun, D., Osborn, T.J., 2009. Modelling seasonality in extreme precipitation: A UK case study. Eur. Phys. J. Spec. Top. 174, 99–111. https://doi.org/10.1140/epjst/e2009-01093-7.

Salazar, A., Baldi, G., Hirota, M., Syktus, J., McAlpine, C., 2015. Land use and land cover change impacts on the regional climate of non-Amazonian South America: A review. Glob. Planet. Change 128, 103–119. https://doi.org/10.1016/j.gloplacha.2015.02.009.

Schmaltz, E.M., Mergili, M., 2018. Integration of root systems into a GIS-based slip surface model: computational experiments in a generic hillslope environment. Landslides 15, 1561–1575. https://doi.org/10.1007/s10346-018-0970-8.

Schmaltz, E.M., Steger, S., Glade, T., 2017. The influence of forest cover on landslide occurrence explored with spatio-temporal information. Geomorphology 290, 250–264. https://doi.org/10.1016/j.geomorph.2017.04.024.

Schmidt, M., Glade, T., 2003. Linking global circulation model outputs to regional geomorphic models: A case study of landslide activity in New Zealand. Clim. Res. 25, 135–150. https://doi.org/10.3354/cr025135.

Segoni, S., Piciullo, L., Gariano, S.L., 2018. A review of the recent literature on rainfall thresholds for landslide occurrence. Landslides 15, 1483–1501. https://doi.org/10.1007/s10346-018-0966-4.

Segoni, S., Pappafico, G., Luti, T., Catani, F., 2020. Landslide susceptibility assessment in complex geological settings: sensitivity to geological information and insights on its parameterization. Landslides 17, 2443–2453. https://doi.org/10.1007/s10346-019-01340-2.

Seneviratne, S.I., Nicholls, N., Easterling, D., Goodess, C.M., Kanae, S., Kossin, J., Luo, Y., Marengo, J., Mc Innes, K., Rahimi, M., Reichstein, M., Sorteberg, A., Vera, C., Zhang, X., Rusticucci, M., Semenov, V., Alexander, L. V., Allen, S., Benito, G., Cavazos, T., Clague, J., Conway, D., Della-Marta, P.M., Gerber, M., Gong, S., Goswami, B.N., Hemer, M., Huggel, C., Van den Hurk, B., Kharin, V. V., Kitoh, A., Klein Tank, A.M.G., Li, G., Mason, S., Mc Guire, W., Van Oldenborgh, G.J., Orlowsky, B., Smith, S., Thiaw, W., Velegrakis, A., Yiou, P., Zhang, T., Zhou, T., Zwiers, F.W., 2012. Changes in climate extremes and their impacts on the natural physical environment, in: Managing the Risks of Extreme Events and Disasters to Advance Climate Change Adaptation: Special Report of the Intergovernmental Panel on Climate Change. https://doi.org/10.1017/CBO9781139177245.006.

Shou, K.J., Lin, J.F., 2020. Evaluation of the extreme rainfall predictions and their impact on landslide susceptibility in a sub-catchment scale. Eng. Geol. 265, 105434. https://doi.org/10.1016/j.enggeo.2019.105434.

Shou, K.J., Yang, C.M., 2015. Predictive analysis of landslide susceptibility under climate change conditions - A study on the Chingshui River Watershed of Taiwan. Eng. Geol. 192, 46–62. https://doi.org/10.1016/j.enggeo.2015.03.012.

Shu, H., Hürlimann, M., Molowny-Horas, R., González, M., Pinyol, J., Abancó, C., Ma, J., 2019. Relation between land cover and landslide susceptibility in Val d'Aran, Pyrenees (Spain): Historical aspects, present situation and forward prediction. Sci. Total Environ. 693, 133557. https://doi.org/10.1016/j.scitotenv.2019.07.363.

Speich, M.J.R., Zappa, M., Scherstjanoi, M., Lischke, H., 2020. FORests and HYdrology under Climate Change in Switzerland v1.0: A spatially distributed model combining hydrology and forest dynamics. Geosci. Model Dev. 13, 537–564. https://doi.org/10.5194/gmd-13-537-2020.

Taylor, K.E., Stouffer, R.J., Meehl, G.A., 2012. An overview of CMIP5 and the experiment design. Bull. Am. Meteorol. Soc. 93, 485–498. https://doi.org/10.1175/BAMS-D-11-00094.1.

Teutschbein, C., Seibert, J., 2012. Bias correction of regional climate model simulations for hydrological climate-change impact studies: Review and evaluation of different methods. J. Hydrol. 456–457, 12–29. https://doi.org/10.1016/j.jhydrol.2012.05.052.

Tofani, V., Bicocchi, G., Rossi, G., Segoni, S., D'Ambrosio, M., Casagli, N., Catani, F., 2017. Soil characterization for shallow landslides modeling: a case study in the Northern Apennines (Central Italy). Landslides 14, 755–770. https://doi.org/10.1007/s10346-017-0809-8.

Tong, Y., Gao, X., Han, Z., Xu, Y., Xu, Y., Giorgi, F., 2021. Bias correction of temperature and precipitation over China for RCM simulations using the QM and QDM methods. Clim. Dyn. 57, 1425–1443. https://doi.org/10.1007/s00382-020-05447-4.

USDA, 1986. Urban hydrology for small watersheds. Technical release 55.National Resources Conservation Service. National Resources Conservation Service.

USDA, 2007. National Engineering Handbook: Part 630 - Chapter 7: Hydrologic Soil Groups. National Resources Conservation Service, National Resources Conservation Service.

Van Beek, L.P.H.H., Van Asch, T.W.W.J., 2004. Regional Assessment of the Effects of Land-Use Change on Landslide Hazard By Means of Physically Based Modelling. Nat. Hazards 31, 289–304. https://doi.org/10.1023/B:NHAZ.0000020267.39691.39.

Vanacker, V., Vanderschaeghe, M., Govers, G., Willems, E., Poesen, J., Deckers, J., Bievre, B.D., 2003. Linking hydrological, infinite slope stability and land-use change models through GIS for assessing the impact of deforestation on slope stability in high Andean watersheds. Geomorphology 52, 299–315. https://doi.org/10.1016/S0169-555X(02)00263-5.

Wang, Y., Liu, J., Yan, S., Yu, L., Yin, K., 2017. Estimation of probability distribution of shear strength of slip zone soils in Middle Jurassic red beds in Wanzhou of China. Landslides 14, 2165–2174. https://doi.org/10.1007/s10346-017-0890-z.

Wang, A., Price, D.T., Arora, V., 2006. Estimating changes in global vegetation cover (1850–2100) for use in climate models. Global Biogeochem. Cycles 20, GB3028. https://doi.org/10.1029/2005GB002514.

Wilby, R.L., Wigley, T.M.L., 1997. Downscaling general circulation model output: A review of methods and limitations. Prog. Phys. Geogr. 21, 530–548. https://doi.org/10.1177/030913339702100403.

Xiao, J., Shen, Y., Ge, J., Tateishi, R., Tang, C., Liang, Y., Huang, Z., 2006. Evaluating urban expansion and land use change in Shijiazhuang, China, by using GIS and remote sensing. Landsc. Urban Plan. 75, 69–80. https://doi.org/10.1016/j.landurbplan.2004.12.005.

Xiao, T., Yin, K., Yao, T., Liu, S., 2019. Spatial prediction of landslide susceptibility using GIS-based statistical and machine learning models in Wanzhou County, Three Gorges Reservoir. China. Acta Geochim. 38, 654–669. https://doi.org/10.1007/s11631-019-00341-1.

UPC, 2021. EASY BAL Software. https://h2ogeo.upc.edu/en/investigation-hydrogeology/software/147-easy-bal-en (accessed on 16 September 2021).

Xu, J., Xu, M., Xi, J., Remedio, A., Sein, D. V., Koldunov, N., Jacob, D., 2016. The Assessment of Surface Air Temperature and Precipitation Simulated by Regional Climate Model REMO over China. Clim. Chang. Res. 12, 286–293. https://doi.org/10.12006/j.issn.1673-1719.2015.194 (in Chinese with English abstract).

Xu, Y., Gao, X., Giorgi, F., Zhou, B., Shi, Y., Wu, J., Zhang, Y., 2018. Projected Changes in Temperature and Precipitation Extremes over China as Measured by 50-yr Return Values and Periods Based on a CMIP5 Ensemble. Adv. Atmos. Sci. https://doi.org/10.1007/s00376-017-6269-1.

Yang, K., He, J., 2019. China meteorological forcing dataset (1979-2018). National Tibetan Plateau Data Center. https://doi.org/10.11888/AtmosphericPhysics.tpe.249369.file.

Zhang, P., Shao, G., Zhao, G., Le Master, D.C., Parker, G.R., Dunning, J.B., Li, Q., 2000. China's forest policy for the 21st century. Science 288, 2135–2136. https://doi.org/10.1126/science.288.5474.2135.